Front. Phys. 11(3), 118103 (2016)
DOI 10.1007/s11467-016-0560-y

REVIEW ARTICLE

Properties of spin–orbit-coupled Bose–Einstein condensates

Yongping Zhang[1,*], Maren Elizabeth Mossman[2], Thomas Busch[1], Peter Engels[2,†], Chuanwei Zhang[3,‡]

[1] *Quantum Systems Unit, Okinawa Institute of Science and Technology Graduate University, Onna, Okinawa 904-0495, Japan*
[2] *Department of Physics and Astronomy, Washington State University, Pullman, WA 99164, USA*
[3] *Department of Physics, The University of Texas at Dallas, Richardson, TX 75080, USA*
*Corresponding authors. E-mail: * yongpingzhang11@gmail.com, † engels@mail.wsu.edu, ‡ Chuanwei.Zhang@utdallas.edu*
Received January 20, 2016; accepted February 18, 2016

The experimental and theoretical research of spin–orbit-coupled ultracold atomic gases has advanced and expanded rapidly in recent years. Here, we review some of the progress that either was pioneered by our own work, has helped to lay the foundation, or has developed new and relevant techniques. After examining the experimental accessibility of all relevant spin–orbit coupling parameters, we discuss the fundamental properties and general applications of spin–orbit-coupled Bose–Einstein condensates (BECs) over a wide range of physical situations. For the harmonically trapped case, we show that the ground state phase transition is a Dicke-type process and that spin–orbit-coupled BECs provide a unique platform to simulate and study the Dicke model and Dicke phase transitions. For a homogeneous BEC, we discuss the collective excitations, which have been observed experimentally using Bragg spectroscopy. They feature a roton-like minimum, the softening of which provides a potential mechanism to understand the ground state phase transition. On the other hand, if the collective dynamics are excited by a sudden quenching of the spin–orbit coupling parameters, we show that the resulting collective dynamics can be related to the famous Zitterbewegung in the relativistic realm. Finally, we discuss the case of a BEC loaded into a periodic optical potential. Here, the spin–orbit coupling generates isolated flat bands within the lowest Bloch bands whereas the nonlinearity of the system leads to dynamical instabilities of these Bloch waves. The experimental verification of this instability illustrates the lack of Galilean invariance in the system.

Keywords atomic Bose–Einstein condensate, spin–orbit coupling, collective excitations, optical lattice

PACS numbers 71.70.Ej, 03.75.Kk, 03.75.Mn, 37.10.Jk

Contents

*Special Topic: Artificial Gauge Field in Ultra-Cold Atomic Gases (Eds. Shuai Chen, Carlos SadeMelo, Chuanwei Zhang & Peng Zhang).

Frontiers of Physics

1 Introduction

Ultracold atoms are charge neutral, therefore the intrinsic physics relevant to the charge degree of freedom of particles is absent in these systems. Ever since Bose-Einstein condensation (BEC) was achieved in atomic gases, one of the main tasks for both theory and experiment has been to artificially introduce charge physics into neutral atoms. The most famous examples of such physics are the Lorentz force effect in a magnetic field and quantum mechanical spin–orbit coupling (SOC). These effects are ultimately related to gauge-dependent vector potentials and are of particular interest in the investigation of ultracold atoms. The connection between the superfluidity of atoms and the so-called synthetic magnetic field or SOC clearly has the potential to generate significant new knowledge and results.

Experimentally, the first artificial magnetic field was synthesized in a harmonically trapped BEC through the rotation of the external trapping potential [1]. In the rotating frame, this leads to a Lorentz force and an anti-trapping potential for atoms, where the force amplitude and the frequency of the anti-trap are proportional to the rotation frequency. However, this technique is limited because the strength of the anti-trap cannot exceed the trapping potential, which implies that it cannot be used for spatially homogeneous BECs. In this case, the magnetic field has to be generated artificially, which can be done using the interactions between laser fields and internal energy states of atoms [2]. The momentum exchange during this interaction gives the atom a finite quasimomentum in a dressed-state basis, which corresponds to a vector potential. Due to the inhomogeneity of the laser field or the external magnetic field gradient, this potential could be spatially dependent, which naturally leads to an artificial magnetic field. In principle, the magnitude of this field is unlimited.

Recently, the first experiments where atoms in two-dimensional (2D) optical lattices are subjected to an artificial magnetic field were reported [3, 4]. In these experiments, the hopping between neighboring sites along one dimension (1D) is assisted by external laser beams through an absorption and stimulated emission process, which results in a spatial inhomogeneity of the phase during the hopping due to momentum kicks. The inhomogeneous phase can accumulate to a finite value around a unit plaquette, which mimics a magnetic flux. It has been shown that the magnetic fields generated in this way allow for staggered (i.e., neighboring plaquettes possess an opposite sign of the magnetic field) [5] or homogeneous [3, 4] fields. Furthermore, the magnitude of the magnetic field is very large in comparison with the same flux in solid-state systems. Today it is generally accepted that the presence of artificial magnetic fields in different environments can significantly change the behavior of atoms and can open many avenues to explore the interplay of superfluidity and magnetic fields in a controllable way.

The research interest in SOC ultracold atoms is, on one hand, strongly motivated by the fundamental role of SOC in many important phenomena in condensed matter physics [6, 7], such as the spin Hall effect [8]. On the other hand, it is stimulated by the fundamental and exotic physics of SOC superfluids. The study of SOC ultracold atomic systems can be divided into two stages, separated by the benchmark experiment of Ian Spielman's group at the National Institute of Standards and Technology (NIST) in 2011 [9]. Before this experiment, most research efforts focused on theoretical proposals regarding the implementation of SOC in ultracold atoms and the physical effects on the single particle level. Some well-known results were the proposal to realize Rashba SOC in an atomic tripod scheme [10] and the use of SOC atoms to simulate spin-Hall physics [11, 12]. Only a few studies had considered SOC in many-body systems [13–15]. Since 2011, the bulk of the attention has shifted to systems combining SOC and many-body effects. The latter originate from the elastic collisions between individual atoms and are required for the existence of superfluidity. The NIST experiment opened the door to the new research topic of SOC superfluids in ultracold bosonic gases, which has no analog in condensed matter, where particles are usually fermionic. Whereas SOC in superconductors is a very interesting topic, the experimental implementation remains a challenge. However, SOC in the Bardeen–Cooper–Schrieffer (BCS) phase of an atomic, degenerate Fermi gas can provide an experimentally accessible platform to explore such systems.

In recent years, the number of research groups involved in experimental and theoretical work on SOC in BECs has increased significantly, and many aspects of these systems have been thoroughly explored. After the first realization of a SOC BEC in ^{87}Rb, the NIST group used this system to explore partial wave scattering [16] and the phenomenon of Zitterbewegung (ZB) [17], to simulate spin Hall physics [18], and to gain control over the tunability of the SOC strength [19]. A University of Science and Technology of China (USTC) group measured the dipole oscillation in different phases of a SOC ^{87}Rb BEC [27], clarified finite temperature effects

on the phase transition [28], measured roton-like collective excitations [29], and recently realized 2D SOC for bosons [30]. The Shanxi University group carried out experiments of both SOC BECs and Fermi gases. In their bosonic ^{87}Rb BEC, they explored the dynamics of loading a BEC into a gauge potential [31]. They performed the first SOC degenerate Fermi gas experiment using ^{40}K, where they quantified the collective properties by measuring the spin dynamics and the momentum distribution, and determined the Fermi surface [32]. They also developed a radio-frequency spectroscopy technique [33], and showed that molecules can be formed with the help of Feshbach resonances [34]. Very recently, they realized 2D SOC [35] for the first time in Fermi gases and observed the band-gap opening around the Dirac point by inducing a perpendicular Zeeman field [36]. The Massachusetts Institute of Technology (MIT) group performed spin-injection spectroscopy in a SOC Fermi gas with ^{6}Li atoms to measure the energy spectrum of SOC and the coexistence of SOC with a Zeeman lattice generated by a radio-frequency field [20]. The Washington State University (WSU) group investigated the physics of the ZB effect in ^{87}Rb [21], realized the Dicke model and the Dicke phase transition [22], measured the collective excitation spectrum (indicating the existence of roton-like structures) [23], and demonstrated the lack of Galilean invariance in SOC systems by measuring dynamical instabilities of a BEC in a moving optical lattice [24]. The Purdue group used a SOC ^{87}Rb BEC to study the physics of Landau–Zener tunneling [25] and to implement interferometry by periodically modulating the power of the laser beams that generate SOC [26]. Finally, the Institute of Physics (IOP) group in Beijing generated SOC in a BEC of ^{87}Rb atoms by modulating magnetic field gradients [37].

Theoretical work has focused on several other aspects, with one of them being the possibility for the energy spectrum to possess several global minima. In a linear system, any superposition of the occupations in these minima is degenerate, which is the basis for many exotic phenomena when atomic interactions are taken into account [38, 39]. In the case of a BEC, the degeneracy is broken by the mean-field energy, and the competition between the mean-field energy and SOC gives rise to new phases and phase transitions. The most famous example of this is the existence of a stripe phase that is an equal superposition of two minima in momentum space [40]. The ground state and collective excitations of SOC BECs have been investigated for a large number of different settings, such as homogeneous [40–49], harmonic [50–54], in the presence of a periodic optical lattice [55–72], a double-well [73–75], rotation [76–81], inside an optical cavity [82–86], and for particles with dipolar interaction [87–92]. For degenerate Fermi gases, the role of SOC in the BEC–BCS crossover region has attracted a lot of attention [93–95]. In the BCS phase, unconventional states are predicted, such as Fulde-Ferrell-Larkin-Ovchinnikov (FFLO) superfluids [38]. Even though the field only started very recently, it has developed in a rapid fashion and several review articles on specific topics along this direction already exist [38, 39, 64, 96–102].

In the following, we will review recent theoretical and experimental progress in this area pioneered by our relevant studies [21–24, 52, 103, 104]. To set the stage, we will first briefly describe the experimental approaches to generate SOC [9, 16–29, 31–35].

2 Spin–orbit coupling in single particle systems

2.1 Experimental realization of spin–orbit coupling

In a typical experiment, a degenerate cloud of ^{87}Rb atoms is prepared in a crossed optical dipole trap. By applying a homogeneous magnetic bias field along the x-direction (as shown in Fig. 1), the $F = 1$ ground state is split into three energy levels, $m_f = 0, \pm 1$, with the energy splittings between them approximately equal within the range of the linear Zeeman effect. Two Raman lasers, whose projection on x-direction point oppositely (see Fig. 1), are used to couple the energy levels $|F = 1, m_f = -1\rangle$ and $|F = 1, m_f = 0\rangle$, and $|F = 1, m_f = 0\rangle$ and $|F = 1, m_f = 1\rangle$. The energy levels can be interpreted as pseudo-spins. However, to simulate a spin-1/2 system, the third energy level has to be moved out of resonance. This can be achieved by using a large magnetic bias field, usually around 10 Gauss, so that the quadratic Zeeman effect shifts the energy splitting between $|F = 1, m_f = -1\rangle$ and $|F = 1, m_f = 0\rangle$ to a larger value than that of the $|F = 1, m_f = 0\rangle$ and $|F = 1, m_f = 1\rangle$ transitions. Choosing an appropriate frequency difference between the Raman lasers then al-

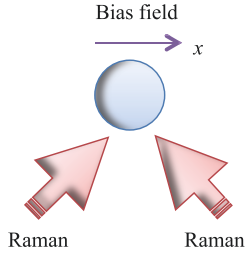

Fig. 1 Experimental scheme for realization of synthetic SOC. The atoms are subjected to a bias magnetic field along the x direction. Two Raman lasers, separated by a $\pi/2$ angle, are incident on the atoms at 45° and 135° with the x direction.

lows one to address only the $|F=1,m_f=-1\rangle$ and $|F=1,m_f=0\rangle$ transition.

The single particle Hamiltonian in the presence of the above Raman coupling is given by

$$H=\frac{p_x^2}{2m}+\frac{\Delta E}{2}\sigma_z+\frac{\hbar\Omega}{2}\cos(2k_{\rm Ram}x-\Delta\omega t)\sigma_x, \quad (1)$$

where p_x is the momentum of atoms along the x direction and m is the mass of atoms. The energy splitting between the $|F=1,m_f=-1\rangle$ and the $|F=1,m_f=0\rangle$ states is given by ΔE, and they are coupled by the effective field $\cos(2k_{\rm Ram}x-\Delta\omega t)$, where $k_{\rm Ram}$ is the projected wavenumber of Raman laser along the counter propagating direction, x. The frequency difference between the two Raman beams is given by $\Delta\omega$ and the coupling coefficient, called the Rabi frequency, is defined as

$$\Omega=\frac{\Omega_1\Omega_2}{2\Delta}. \quad (2)$$

This relates the Rabi frequency of each Raman beam, $\Omega_{1,2}$, to the single photon detuning Δ. The Pauli matrices are used in their standard notation as $\{\sigma_x,\sigma_y,\sigma_z\}$. The wave function of the system can be written as $\Phi(x)=(\Phi_\uparrow,\Phi_\downarrow)^T$, where the hyperfine states are relabeled as

$$|\uparrow\rangle=|F=1,m_f=0\rangle,\quad |\downarrow\rangle=|F=1,m_f=-1\rangle. \quad (3)$$

Using the standard rotating wave approximation, the Hamiltonian can be written as $H=p_x^2/(2m)+\Delta E\sigma_z/2+\hbar\Omega\cos(2kx-\Delta\omega t)\sigma_x/2-\hbar\Omega\sin(2kx-\Delta\omega t)\sigma_y/2$. In the co-rotating frame of the effective field, a unitary transformation, $U=\exp[{\rm i}(k_{\rm Ram}x-\Delta\omega t/2)\sigma_z]$, can be applied to give

$$\begin{aligned}H&=U^\dagger HU-{\rm i}\hbar U^\dagger\frac{\partial U}{\partial t}\\&=\frac{(p_x+\hbar k_{\rm Ram}\sigma_z)^2}{2m}+\frac{\Delta E-\hbar\Delta\omega}{2}\sigma_z+\frac{\hbar\Omega}{2}\sigma_x. \quad (4)\end{aligned}$$

After dropping a constant term, the Hamiltonian relevant for the experimental SOC can be written as

$$H_{\rm soc}=\frac{p_x^2}{2m}+\gamma p_x\sigma_z+\frac{\hbar\delta}{2}\sigma_z+\frac{\hbar\Omega}{2}\sigma_x, \quad (5)$$

where $\delta=\Delta E/\hbar-\Delta\omega$ is the detuning and the SOC strength is defined by

$$\gamma=\frac{\hbar k_{\rm Ram}}{m}. \quad (6)$$

2.2 Tunable spin–orbit coupling

To understand the relevance of the above Hamiltonian, we discuss the experimental implementation of the tunable parameters γ, δ, and Ω.

- *Detuning.* Detuning relates to the energy splitting and the frequency difference between the Raman lasers, $\delta=\Delta E/\hbar-\Delta\omega$. Because the energy splitting is proportional to the amplitude of the bias magnetic field, one way to adjust the detuning is by changing the bias field. In particular, a spatially in-homogeneous bias field can be used to make the detuning also spatially dependent [2]. Furthermore, the detuning can also be changed by adjusting the frequency difference between the Raman beams. This is possible to do dynamically during an experiment.
- *Rabi frequency.* The Rabi frequency, $\Omega=\Omega_1\Omega_2/(2\Delta)$, is proportional to the single photon Rabi frequency, $\Omega_{1,2}\propto\sqrt{I_{1,2}}$, where $I_{1,2}$ are the intensities of the Raman beams. It can therefore be adjusted easily by changing the power of each Raman beam. This control is coherent and can be used in real time during an experiment.
- *Spin–orbit coupling strength.* The SOC strength, $\gamma=\hbar k_{\rm Ram}/m$, relates to the projected wave number of the Raman beams, $k_{\rm Ram}$. To tune the strength of γ, one can naively consider changing the angle between the incident Raman lasers (see Fig. 1), which changes $k_{\rm Ram}$. However, in a real experiment this possibility is very limited due to restrictions on optical alignment and optical accessibility. Once the setup is fixed, it is typically not possible to change the angle dynamically.

However, the SOC strength can be changed effectively by periodic modulation of the power of the Raman lasers [103]. This leads to

$$\Omega=\Omega_0+\tilde{\Omega}\cos(\omega t), \quad (7)$$

where Ω_0 is the average value of the Rabi frequency and $\tilde{\Omega}$ is the modulation amplitude. This expression assumes that the modulation frequency, ω, is much larger than any other energy scale in the system, such that it cannot follow or respond. This suggests a unitary transformation to cancel the modulation term in the Rabi frequency by using

$$U_1(t)=\exp\left(-{\rm i}\frac{\tilde{\Omega}\sin(\omega t)}{2\omega}\sigma_x\right), \quad (8)$$

which leads to

$$\begin{aligned}H_{\rm eff}&=U_1^\dagger H_{\rm soc}U_1-{\rm i}\hbar U_1^\dagger\frac{\partial U_1}{\partial t}\\&=\frac{p_x^2}{2m}+\left(\frac{\hbar\delta}{2}+\gamma p_x\right)\cos\left[\frac{\tilde{\Omega}}{\omega}\sin(\omega t)\right]\sigma_z\\&\quad+\frac{\hbar\Omega_0}{2}\sigma_x+\left(\frac{\hbar\delta}{2}+\gamma p_x\right)\sin\left[\frac{\tilde{\Omega}}{\omega}\sin(\omega t)\right]\sigma_y. \quad (9)\end{aligned}$$

Using the standard Bessel function relation $\exp(\mathrm{i}\tilde{\Omega}\sin(\omega t)/\omega) = \sum_n J_n(\tilde{\Omega}/\omega)\exp(\mathrm{i}n\omega t)$, where J_n is the nth Bessel function of the first kind, and taking into account the high modulation frequency, one need only keep the zeroth order term ($n = 0$) that does not depend on time. The resulting time-independent Hamiltonian is

$$H_{\mathrm{eff}} = \frac{p_x^2}{2m} + \left(\frac{\hbar\delta}{2} + \gamma p_x\right) J_0\left(\frac{\tilde{\Omega}}{\omega}\right)\sigma_z + \frac{\hbar\Omega_0}{2}\sigma_x, \quad (10)$$

with a modified SOC strength of the form

$$\gamma_{\mathrm{eff}} = \gamma J_0\left(\frac{\tilde{\Omega}}{\omega}\right). \quad (11)$$

The high frequency modulation of the power of Raman beams can therefore effectively tune the SOC strength. We note that this modulation modifies the detuning in the same manner

$$\delta_{\mathrm{eff}} = \delta J_0\left(\frac{\tilde{\Omega}}{\omega}\right). \quad (12)$$

Here, we make a number of comments on this method.

- The above method is coherent and can be used dynamically. If the change in the modulated amplitude of $\tilde{\Omega}$ is slow compared to the high frequency ω, the time dependence of the effective spin–orbit coupling strength is given by $\gamma_{\mathrm{eff}}(t) = \gamma J_0(\tilde{\Omega}(t)/\omega)$.
- The described approach has been adopted and shown to work in a recent experiment by the NIST group [19]. However, to modify the strength, the value of $\tilde{\Omega}$ can potentially exceed that of Ω_0, which means that $\Omega = \Omega_0 + \tilde{\Omega}\cos(\omega t) < 0$ for every half period of modulation. In the experiment [19], the power modulation of the Raman beams alone could not change the sign of the Rabi frequency. To do this nevertheless, one can modify the relative phase between the two Raman beams such that for every half period the relative phase jumps by π. If the two Raman beams are in-phase, Ω_1 and Ω_2 have the same sign, whereas if they are out of phase, Ω_1 and Ω_2 have opposite signs. Using high frequency modulation and phase jumping every half period, the NIST group showed that the SOC strength could be tuned according to γ_{eff} for a nonzero δ [19].
- Finally, the above analysis focused on the linear regime without considering the mean-field interactions between the atoms in a BEC. However, one may wonder about the effects of the interactions on the high frequency modulation of the Rabi frequency. Today, all SOC BEC experiments have been performed using ^{87}Rb, where the difference in the interaction strength between the $|F = 1, m_f = 0\rangle$ and $|F = 1, m_f = -1\rangle$ states and within each component is very small and does not lead to any observable consequences. One can then assume, to a good approximation, that these condensates have $SU(2)$ symmetry (i.e., the interactions do not depend on the spins) and are therefore not affected by the spin-dependent unitary transformation in Eq. (8). However, if the symmetry is broken and the interaction values do not coincide, the high frequency modulation would be affected by the nonlinearity.

3 Trapped BEC with spin–orbit coupling: Ground states and collective excitations

In this section, we will review different aspects of the ground state and collective excitations for experimentally realizable SOC BECs. We show that such systems can be mapped to the Dicke model [22, 103], which is a far-reaching and powerful model in quantum mechanics.

3.1 Ground states of SOC BEC and analogy to the Dicke model

3.1.1 Theory

To describe the ground state properties of an experimentally realizable SOC BEC, we study a 2D geometry as shown in Fig. 2(a). Such reduced dimensions can be achieved by applying a strong trapping potential in the z direction. The reason that we adopt the 2D geometry is that it provides an opportunity in a later section to study scissors and quadruple modes in a clean setting. The two Raman lasers are counter-propagating along the x-direction to couple the two hyperfine ground states of ^{87}Rb atoms through a two-photon process [see Fig. 2(b)] and a very large single photon detuning Δ ensures that the excited state can be adiabatically eliminated. Only the ground state levels are involved in the two-photon process.

To determine the ground state properties, we use a mean-field approach in the form of the standard Gross–Pitaevskii (GP) equation

$$\mathrm{i}\hbar\frac{\partial\Phi}{\partial t} = [H_{\mathrm{2D}} + V(x, y) + H_{\mathrm{int}}]\,\Phi, \quad (13)$$

where the single particle, SOC part is given by

$$H_{\mathrm{2D}} = \frac{p_x^2}{2m} + \frac{p_y^2}{2m} + \gamma_{\mathrm{eff}} p_x\sigma_z + \frac{\hbar\Omega}{2}\sigma_x. \quad (14)$$

For simplicity, we restrict the treatment to the case of zero detuning, $\delta = 0$. Ω in Eq. (14) should be equal to

Ω_0 of Eq. (10). If there is no high frequency modulation of the Rabi term, $\gamma_{\rm eff} \to \gamma$. The 2D trapping potential is chosen to be harmonic

$$V(x,y) = \frac{1}{2} m\omega_{y^2}(\eta^2 x^2 + y^2), \tag{15}$$

where ω_x and ω_y are the trapping frequency along the x- and y-direction, respectively, and the ratio between them is given by $\eta = \omega_x/\omega_y$. The term describing the inter-atomic interactions in Eq. (13) is given by

$$H_{\rm int} = \begin{pmatrix} g_{\uparrow\uparrow}|\Phi_\uparrow|^2 + g_{\uparrow\downarrow}|\Phi_\downarrow|^2 & 0 \\ 0 & g_{\uparrow\downarrow}|\Phi_\uparrow|^2 + g_{\downarrow\downarrow}|\Phi_\downarrow|^2 \end{pmatrix}, \tag{16}$$

where the coefficients g relates to the respective s-wave scattering lengths. In the real experiment on ^{87}Rb, the difference between $g_{\uparrow\uparrow}$, $g_{\uparrow\downarrow}$ and $g_{\downarrow\downarrow}$ is very small. To make the numerical calculations more general, we choose to use dimensionless units by scaling energy, length, and time as $\hbar\omega_y$, $\sqrt{\hbar/(m\omega_y)}$, and $1/\omega_y$, respectively.

The ground states of the GP equation can be found by using the standard imaginary time evolution method with a typical result shown in Fig. 2(c). Whereas the density profile of each spin component follows the well-known Thomas-Fermi distribution, the momentum distribution shows the existence of a finite quasimomentum along the propagation direction of the Raman lasers, see Fig. 2(d).

Such a stationary ground state, which has zero group velocity despite possessing a finite quasimomentum, is fundamentally different from the well-known ground states of a BEC in the absence of SOC, which condense at zero quasimomentum. In fact, the nonzero quasimomentum is located close to the minimum of the SOC single-particle spectrum

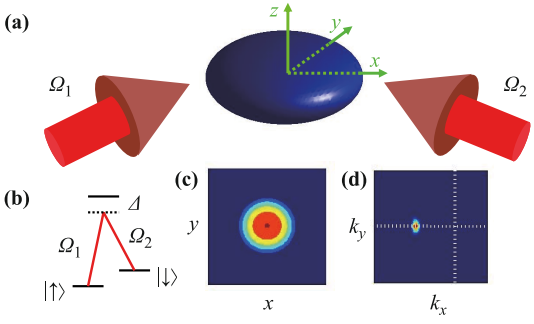

Fig. 2 Experimental scheme for realization of spin–orbit coupling. **(a)** Raman laser geometry. **(b)** Two-photon coupling. **(c)** Typical ground state density distribution of one spin component. **(d)** Corresponding momentum distribution. The horizontal and vertical dotted lines represent $k_y = 0$ and $k_x = 0$ respectively. Reproduced from Ref. [103].

$$E_\pm(k_x,k_y) = \frac{k_x^2 + k_y^2}{2} \pm \sqrt{(\gamma_{\rm eff}k_x)^2 + \left(\frac{\Omega}{2}\right)^2}, \tag{17}$$

where k_x and k_y are the quasimomenta in the x and y direction, respectively. The spectrum $E_\pm(k_x,k_y)$ is the dispersion relation of Eq. (14). One can see that SOC only affects the spectrum along its own direction, x, while keeping the free particle dispersion along the y-direction. One of the main features of this spectrum is that it possesses a double-well structure in its lowest branch: $E_-(k_x,k_y)$. If $\Omega < 2\gamma_{\rm eff}^2$, two degenerate minima appear at $(k_x,k_y) = (\pm k_{\rm min}, 0)$, where

$$k_{\rm min} = \sqrt{\gamma_{\rm eff}^2 - \left(\frac{\Omega}{2\gamma_{\rm eff}}\right)^2}. \tag{18}$$

However, if $\Omega \geq 2\gamma_{\rm eff}$, only one minimum exists at $k_{\rm min} = 0$ and the lowest branch of the single-particle spectrum has the standard parabolic form. The behavior of the ground state in this regime is mostly the same as for BECs in the absence of SOC. In the following, we concentrate on the regime $\Omega < 2\gamma_{\rm eff}^2$, where the ground states spontaneously choose to occupy one of the minima and therefore breaks the degeneracy of the single-particle spectrum. Such a ground state is called a plane wave phase in the literature [40], because the atoms condense at a finite quasimomentum, just like a plane wave.

The tuning of the SOC parameters, Ω or $\gamma_{\rm eff}$, drives the system through a phase transition between the plane wave phase and the conventional BEC phase. The critical value for the transition is given by $\gamma_{\rm eff}^c = \sqrt{\Omega/2}$ and it can be characterized using the spin polarizations

$$\langle\sigma_z\rangle = \int {\rm d}x{\rm d}y\ (|\Phi_\uparrow|^2 - |\phi_\downarrow|^2), \tag{19}$$

and

$$\langle\sigma_x\rangle = \int {\rm d}x{\rm d}y\ \Phi_\uparrow^*\Phi_\downarrow. \tag{20}$$

Because the plane wave phase breaks time-reversal symmetry, which is closely linked to the existence of ferromagnetism, one can expect the spin-imbalance to be $\langle\sigma_z\rangle \neq 0$. This can also be seen by realizing that when $\Omega < 2\gamma_{\rm eff}^2$, SOC dominates and spin polarization is preferred. In the conventional BEC regime, $\Omega \geq 2\gamma_{\rm eff}^2$, the Rabi frequency term dominates and, because it depends on σ_x, the spin-balance $\langle\sigma_z\rangle = 0$ and $\langle\sigma_x\rangle \neq 0$ is preferred.

Results for the numerically obtained ground states as a function of the SOC strength $\gamma_{\rm eff}$ [recalling that $\gamma_{\rm eff}/\gamma = J_0(\tilde{\Omega}/\omega)$] are shown in Fig. 3. Here, the circles represent $|\langle\sigma_z\rangle|$ and the squares $\langle\sigma_x\rangle$. As expected from the intuitive analysis above, the spin polarization $|\langle\sigma_z\rangle|$

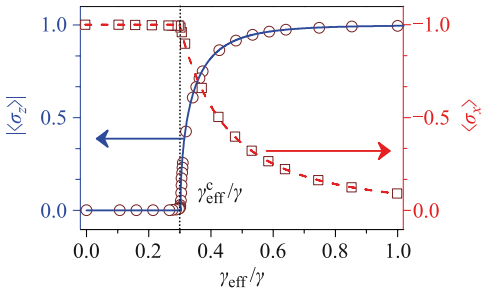

Fig. 3 Quantum phase transition indicated by the spin polarization $|\langle\sigma_z\rangle|$ and $\langle\sigma_x\rangle$ as a function of $\gamma_{\rm eff}$. The solid and dashed lines are from the prediction of the Dicke Hamiltonian, i.e., (25) and (26). The circles and squares are from the numerical simulation of the GP equation (13). $\Omega = 16$, $\gamma = 9.37$. Reproduced from Ref. [103].

is zero for a small $\gamma_{\rm eff}$ (where the Rabi frequency term dominates), whereas beyond the critical value $\gamma_{\rm eff}^c$ (where SOC dominates) it takes a finite value. The quantity $\langle\sigma_x\rangle$ also behaves as expected: it is maximal ($\langle\sigma_x\rangle = 1$) when the Rabi frequency dominates and decreases when SOC dominates with increasing values of $\gamma_{\rm eff}$. The sharp changes in both $\langle\sigma_z\rangle$ and $\langle\sigma_x\rangle$ confirm the phase transition at the critical value $\gamma_{\rm eff}^c = \sqrt{\Omega/2}$. Whereas the plot only gives the absolute value of the spin polarization, it is worth noting that the plane-wave phase ground-state spontaneously occupies one of the two minima in momentum space, which are characterized by opposite signs of $\langle\sigma_z\rangle$.

Because the system possesses one phase in which the spin is balanced and a second in which it is imbalanced, and in which it chooses the sign of the polarization randomly, it closely resembles the Dicke model [105]. Traditionally, the Dicke model describes the interaction between a single quantum field and a two-level atomic ensemble. Besides its fundamental importance, the Dicke model is well known for the presence of an interesting phase transition. Once the strengths of the interaction between the atoms and the quantum field interaction exceeds a threshold value, the atomic ensemble interacts collectively with the quantum field by resembling a large spin. This leads to a so-called superradiant phase in which the photon mode is occupied macroscopically and the spin polarization of the atomic ensemble is nonzero [106]. The sign of the polarization is chosen spontaneously by the ground state. If, on the other hand, the interaction strength is smaller than the threshold value, the spin polarization and the photon mode occupation are zero. The ground state properties of the SOC BEC, as shown in Fig. 3, therefore allow interpreting the system in terms of a Dicke-type transition.

To formally map the SOC system to the Dicke model, we introduce the collective spin operators as

$$S_{(x,y,z)} = \frac{1}{2}\sum_i \sigma^i_{(x,y,z)}, \tag{21}$$

where the sum runs over all atoms. Substituting these into the N-particle Hamiltonian of Eq. (14), and using the harmonic mode operator

$$p_x = \mathrm{i}\sqrt{\frac{m\hbar\omega_x}{2}}(a^\dagger - a), \tag{22}$$

one can obtain the Hamiltonian [103]

$$H_{\rm Dicke} = \hbar\omega_x N a^\dagger a + \hbar\Omega S_x + \mathrm{i}\gamma_{\rm eff}\sqrt{2m\hbar\omega_x}(a^\dagger - a)S_z. \tag{23}$$

This is the Hamiltonian of the Dicke model [105], which can be more clearly seen by introducing $S_+ = S_y + iS_z$ and $S_- = S_y - \mathrm{i}S_z$. The Hamiltonian can then be written as

$$H_{\rm Dicke} = \hbar\omega_x N a^\dagger a + \hbar\Omega S_x + \gamma_{\rm eff}\sqrt{\frac{m\hbar\omega_x}{2}}(a^\dagger - a)(S_+ - S_-). \tag{24}$$

Note that we already neglected the dynamics along the y-direction, because it is not effected by SOC and therefore does not provide new physics.

For $\gamma_{\rm eff} > \sqrt{\Omega/2}$ the analytical results predicted by the Dicke model of Eq. (24) can be written as [103, 106]

$$|\langle\sigma_z\rangle| = \frac{2}{N}|S_z| = \sqrt{1 - \frac{\Omega^2}{4\gamma_{\rm eff}^4}}, \tag{25}$$

$$\langle\sigma_x\rangle = \frac{2}{N}S_x = -\frac{\Omega}{2\gamma_{\rm eff}^2}, \tag{26}$$

and if $\gamma_{\rm eff} \le \sqrt{\Omega/2}$, they are $|\langle\sigma_z\rangle| = 0$ and $\langle\sigma_x\rangle = -1$. These analytical results are also shown in Fig. 3, using a solid line for $|\langle\sigma_z\rangle|$ and a dash one for $\langle\sigma_x\rangle$. The perfect match between these two approaches confirms the validity of the mapping to the Dicke model. Because the Dicke phase transition is of second order, the SOC phase transition is of second order as well. This can also be seen easily by calculating the energy numerically.

Let us finally comment on the effects of the interactions and the existence of other possible ground states.

- *Interaction effects.* In the above mapping, the interactions given in Eq. (16) play a fundamental role, even though they do not explicitly appear in the derivation. In an interacting BEC all atoms are forced to occupy the same many-body ground state, which allows the restriction to a single quantum mode, a, of the harmonic oscillator, $p_x \to a^\dagger - a$, to mimic the single mode quantum field of the Dicke

model. If the interaction is absent, the atoms do not affect each other, and therefore each atom behaves independently. This makes it impossible to use only a single harmonic mode. A direct effect of the use of a single mode is that in Eqs. (25) and (26) the spin average of the BEC is proportional to $1/N$ times the collective spin value, i.e., $|\langle\sigma_z\rangle| = 2|S_z|/N$. The physics of a single-particle SOC is therefore fundamentally different from Dicke physics.

The reason that the interaction terms do not explicitly appear in the derivation of the Dicke model as given in Eq. (24), is that the difference between the spin-dependent interaction coefficients ($g_{\uparrow\uparrow}$, $g_{\uparrow\downarrow}$, and $g_{\downarrow\downarrow}$) is very small in current experiments. This makes any spin twist effect, which is proportional to $(g_{\uparrow\uparrow}+g_{\downarrow\downarrow}-2g_{\uparrow\downarrow})S_z^2$, negligible. However, if the spin-dependent interaction strengths are unequal, the spin twist effect needs to be included in the derivation of the Dicke Hamiltonian.

- *Other possible ground states.* The plane wave phase exists in the parameter regime where the single-particle spectrum of the spin–orbit coupling has a double-well structure in momentum space. However, in this regime, a second ground state phase can appear and, using a simple variational method, a striped phase [40] has been predicted for currently experimentally realizable SOC BECs [41, 43]. This striped phase is characterized by the equal occupation of the two minima at the same time and it features a spatially periodic density modulation. Unfortunately, for realistic experiments using ^{87}Rb, this phase only exists in the regime of very weak Rabi frequencies, which is hard to reach under current experimental circumstances.

3.1.2 *Experimental realization*

In the previous section, we have reviewed the theoretical work showing that the ground state physics of a SOC BEC can be related to the Dicke model and that the phase transition between the plane wave phase and the conventional BEC phase is a Dicke-type phase transition [103]. In this section, we will describe the experimental confirmation of this model [22].

Let us first stress the importance of the Dicke model [107] and describe the challenges relating to its experimental realization. The Dicke model deals with the interaction between an ensemble of simple two-level atoms and a single quantum field mode, and it is therefore a fundamental model in quantum mechanics. It helps to develop a basic understanding of how many-body systems interact with light and, because this hybrid many-body system is theoretically tractable, it provides an essential platform to explore the collective dynamics of many-body physics. The predicted phase transition is of fundamental significance for investigating collective many-body behavior and helps interpret other effects in many-body systems. Today, the Dicke system is well understood and a broad range of applications have been found in areas such as quantum optics and quantum information. To generate a single quantum mode, usually an optical cavity is used (see Fig. 4). However, to observe the Dicke phase transition, a strong coupling between the optical cavity field and the atoms is required, which until recently was not experimentally possible. Even though the Dicke model was proposed nearly 60 years ago [105], the predicted phase transition was observed experimentally only very recently, using momentum eigenstates of a BEC inside an optical cavity [108].

Compared to the cavity scheme, the proposed approach, using a harmonically trapped and SOC BEC (see Fig. 4), has the advantages of having fully tunable parameters, a very strong coupling, and essentially no dissipation. This makes the SOC BEC an excellent platform for exploring the Dicke model and related applications.

To study experimentally the ground state properties of a SOC BEC and to demonstrate the analogy with the Dicke model, an elongated BEC of ^{87}Rb atoms was prepared in a crossed dipole trap with trapping frequencies $(\omega_x, \omega_y, \omega_x) = 2\pi \times (12 - 34, 134, 178)$ Hz. Then, the Raman lasers, arranged such that the angle between them was $\pi/2$ and the angle between each and the BEC long axis was $\pi/4$, were adiabatically ramped up to dress the atoms. Their frequencies were deliberately chosen to lie between the D1 and D2 lines to minimize the AC stark shift due to single photon processes. A 10 gauss magnetic bias field was applied along the long axis to define a quantum axis and to produce a quadratic Zeeman shift to eliminate the state $|1, 1\rangle$. The samples were measured using a spin-involved time-of-flight technique, which allowed the revelation of spin and momentum distributions.

To change the atomic bare states to Raman dressed states, two experimental approaches were investigated

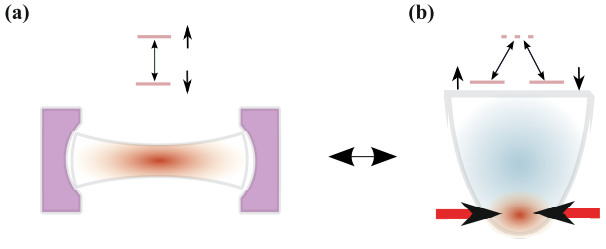

Fig. 4 Experimental schemes for the realization of the Dicke model. **(a)** Optical cavity scheme. The optical model in the cavity couples two atomic spin states. **(b)** Spin–orbit-coupled BEC in an external trap. Two spin states are coupled via a two-photon process. Reproduced from Ref. [22].

in detail. The first started from a BEC in the bare state $|\uparrow\rangle$ (or $|\downarrow\rangle$), and adiabatically turned on the Raman lasers, using a very large detuning. The initial bare states and the dressed states with the large detuning overlap strongly and have a similar spin composition. In the next step, the Raman detuning is adiabatically reduced to a final value. In the second approach, the detuning is kept at the desired value, whereas the Rabi frequency is increased adiabatically by ramping up the Raman lasers. More details can be found in Ref. [22].

The experimental measurements of the spin polarizations of ground states in the plane wave phase and conventional BEC phase are shown in Fig. 5. In the experiment, however, the phase transition is induced by changing the Rabi frequency Ω, rather than the SOC strength, as proposed in the above section. The Rabi frequency is scaled in units of the recoil energy of the Raman lasers, $E_{\rm Ram} = \hbar^2 k_{\rm Ram}^2/(2m)$. Considering this energy scale, the critical condition of the phase transition, $\Omega = 2\gamma_{\rm eff}^2$, is $\Omega = 4E_{\rm Ram}$. In the regime $\Omega < 4E_{\rm Ram}$, the system is in the plane wave phase [see Fig. 5(a)], which is analogous to the superradiant phase of the Dicke model. In this phase, the ground state spontaneously occupies one of the two momentum-space minima [labeled by L and R in Fig. 5(a)]. The solid line is the prediction from the Dicke model given in Eq. (25). One can clearly see that the experimental data agrees well with the prediction. For a typical Rabi frequency, the time-of-flight measurements are shown in Fig. 5(b), where the two spin states are separated by $2\hbar k_{\rm Ram}$. Beside the non-zero spin polarization of the atoms, the photon number is also non-vanishing. Because the mean photon number corresponds to the square of the quasimomentum of the BEC, i.e., q^2 and $q^2 = 1 - \Omega^2/4\gamma_{\rm eff}^2$ according to the prediction from the Dicke Hamiltonian [22], it can be obtained experimentally from the time-of-flight data. The results are shown in Fig. 6(a), together with the data points obtained using numerical solutions of the GP equation and the analogous Dicke model. All results are consistent with each other.

The good agreement of the results regarding the spin polarization of the atoms and the mean photon number, shown in Figs. 5 and 6, therefore confirms that the ground states of a SOC BEC can be used to explore Dicke physics. It is worth noting that in the above treatment the detuning was always zero. If the detuning were chosen to be finite, the phase transition becomes less sharp and the region in which the system is in the plane wave phase (corresponding to the superradiant phase of a generalized Dicke model) is extended, see Fig. 7.

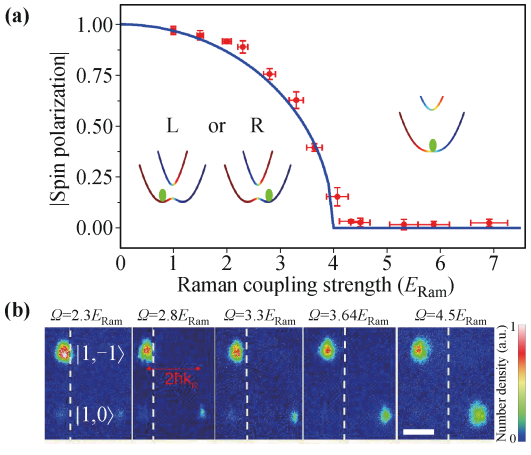

Fig. 5 **(a)** $|\langle\sigma_z\rangle|$ as a function of the Rabi frequency Ω for $\delta = 0$. The solid blue line is from the prediction by the Dicke model. The symbols are the experimentally measured data. The vertical error bars are the standard deviations for 4 to 5 realizations, while the horizontal error bars reflect the systematic uncertainties in the determination of Ω. The insets are examples of the dispersion relation in different phases. **(b)** Experimental time-of-flight images of ground states loaded to $+q$. Due to the Raman momentum transfer, the pseudospin states are horizontally separated by $2\hbar k_{\rm Ram}$. The vertical dashed line represents zero momentum. Reproduced from Ref. [22].

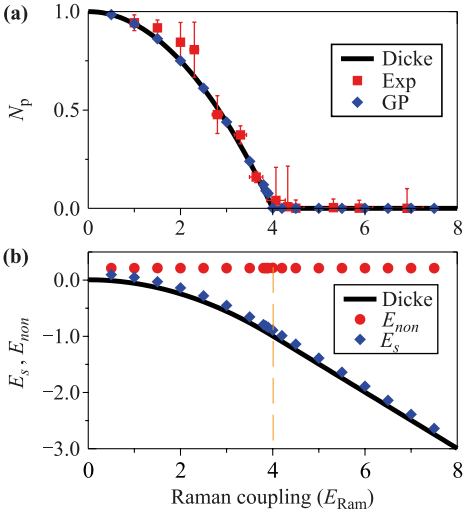

Fig. 6 **(a)** Scaled photon number as a function of Ω. The red symbols are the experimental results from the quasimomentum measurements. The vertical error bars are the standard deviations for 4 to 5 realizations, whereas the horizontal error bars reflect the systematic uncertainties in the determination of Ω. The blue symbols are from the GP equation simulation, and the solid line is from the prediction of the Dicke model. **(b)** Numerical results for the single particle ground state energy E_s (*blue diamonds*) and the nonlinear interaction energy E_{non} (*red circles*) as a function of Ω. The black solid line indicates the single particle energy from the prediction of the Dicke model. The dashed vertical line shows the location of the quantum phase transition. Reproduced from Ref. [22].

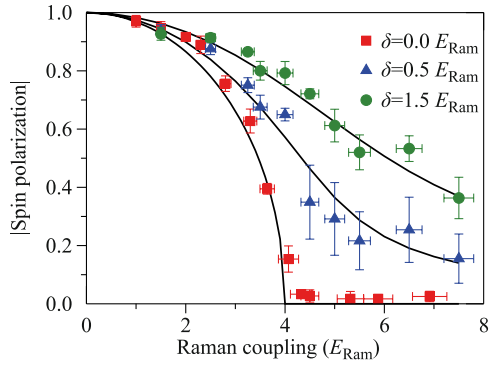

Fig. 7 $|\langle\sigma_z\rangle|$ as a function of Rabi frequency Ω for nonzero δ. For a finite detuning, there is no quantum phase transition. The data points are experimental measurements and the solid lines are the corresponding predictions of the generalized Dicke model. The vertical error bars are the standard deviations for 4 to 5 realizations, whereas the horizontal error bars reflect the systematic uncertainties in the determination of Ω. Reproduced from Ref. [22].

3.2 Collective excitations: Dipole oscillation, scissors mode and quadrupole mode

Inevitably, various physical quantities may change dramatically around the critical point of the quantum phase transition. This provides other signatures that can signify this transition and in the following, we summarize the results for the collective dynamics of the ground states of a SOC BEC. Theoretically and experimentally, it has been shown that the characteristic frequencies of some typical collective dynamical variables behave totally different in different phases.

3.2.1 Dipole oscillation

Dipole oscillations are one of most fundamental collective excitations for a harmonically trapped BEC [110]. To excite a dipole mode, the trap can be suddenly displaced, such that the initial ground state of the BEC is no longer the ground state of the displaced trap. This leads to a collective excitation of the atoms, which for a conventional BEC always oscillates at the trapping frequency. The nonlinearity has no effect on this frequency. Because of this, dipole oscillation can be used to calibrate the trap frequencies experimentally.

In the presence of SOC, however, the period of the dipole oscillation depends on the SOC parameters. This can be seen by numerically tracking the center-of-mass

$$\langle r\rangle = \int \mathrm{d}x\mathrm{d}y\ (|\Phi_\uparrow|^2 + |\Phi_\downarrow|^2)\ r(t) \tag{27}$$

after a sudden shift of the trapping potential. If the displacement of the trapping potential is in the y-direction, the center-of-mass motion $\langle y\rangle$ behaves just like in the case of a regular BEC, with the oscillation frequency being equal to the trapping frequency of ω_y and unaffected by the SOC parameter. However, if the displacement is in the x-direction, i.e., the direction along which the Raman lasers propagate, the SOC strength affects the oscillation period, see Fig. 8. For each value of the Rabi frequency, Ω, the dipole oscillation periods have a peak located around the critical values of Dicke-type phase transition. In the conventional BEC phase (small $\gamma_{\rm eff}$), the period increases with increasing SOC strength, whereas in the plane wave phase (large $\gamma_{\rm eff}$), the period decreases. As expected, without SOC ($\gamma_{\rm eff} = 0$), the period corresponds to the one for a regular BEC, i.e., $T = T_0 = 2\pi/\omega_x$. For values of $\gamma_{\rm eff}$ that are far beyond the critical value $\gamma^c_{\rm eff}$ for the phase transition, the period decreases to T_0 again. This is because, in this region, the ground state consists of only one component. We also note that in the plane wave phase, close to the critical point, the center-of-mass motion suffers from a fast decay, as can be seen from the inset plots in Fig. 8. In any other regime the propagation is without dissipation.

The peaks and the damped motion around $\gamma^c_{\rm eff}$ provide significant experimental signatures for the Dicke-type phase transition. They have been examined more carefully in both experiment [27] and theory [109].

3.2.2 Scissors mode

The scissors mode [110–112], in a fashion similar to that of the dipole mode, can also be used to study the effects of SOC. It can be excited by introducing an anisotropy in the trapping potential (e.g., $\eta = \omega_x/\omega_y \neq 1$), followed by a sudden rotation of the asymmetric trap by an angle θ. This induces a periodic oscillation of the quantity $\langle xy\rangle$,

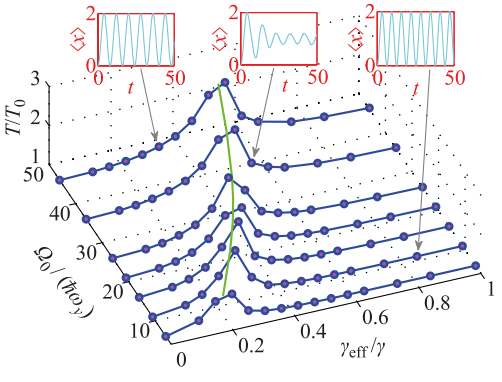

Fig. 8 The period T of the dipole oscillation as a function of the Rabi frequency Ω and the SOC strength. The insets demonstrate the corresponding center-of-mass motion $\langle x\rangle$. The green line is the critical value for the phase transition. The circles are from a numerical simulation of Gross–Pitaevskii equations (GPE). The harmonic trap displacement $D = 1$. $T_0 = 2\pi/\omega_x$. Reproduced from Ref. [103].

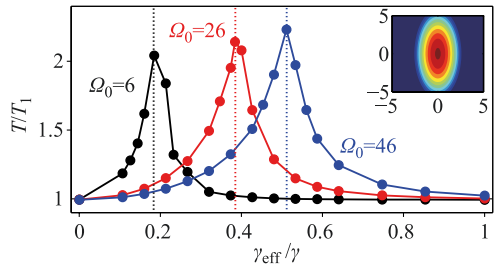

Fig. 9 The oscillation period of the scissors mode as a function of the SOC strength for three different Ω. The scissors mode is excited by a sudden rotation of the asymmetric harmonic trap by an angle θ. $T_1 = 2\pi/\omega_y\sqrt{\eta^2+1}$ is the oscillation period with SOC. In this figure, $\eta = \sqrt{5}$ and $\theta = 4°$. Reproduced from Ref. [103].

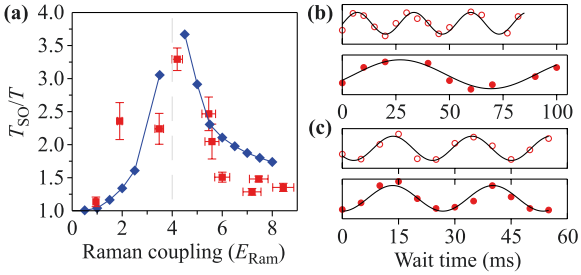

Fig. 10 The quadrupole mode period as a function of Ω. The blue points and the solid blue line are from numerical simulations. The dashed vertical line represents the location of the quantum phase transition. The red symbols with error bars are the experimentally measured data. The vertical error bars are the uncertainty of the oscillation frequency from the sinusoidal fits, whereas the horizontal error bars reflect the systematic uncertainties in the determination of Ω. **(b, c)** Experimentally observed temporal oscillation of the condensate width for **(b)** $\Omega = 4.2E_{\rm Ram}$ and **(c)** $\Omega = 7.2E_{\rm Ram}$. The upper and lower panel of each figure represents the off- resonant case ($\delta \gg \Omega$) and on-resonant case ($\delta \sim 0$), respectively. The solid lines are fits to the experimental data. Reproduced from Ref. [22].

which is defined as

$$\langle xy\rangle = \int \mathrm{d}x\mathrm{d}y\ (|\Phi_\uparrow|^2 + |\Phi_\downarrow|^2)\ xy. \tag{28}$$

For a regular BEC, the period of the scissors mode is given by $T_1 = 2\pi/\sqrt{\omega_x^2+\omega_y^2}$, which was confirmed experimentally [110–112]. In the presence of a spin–orbit coupling, we theoretically find that this period is no longer constant and the dependence on the coupling strength is shown in Fig. 9 for three different Rabi frequencies. Just as for the dipole oscillation, the period of the scissors mode shows peaks and damping of the oscillations around the critical point.

3.2.3 Quadrupole mode

The collective quadrupole oscillations have also been investigated theoretically and experimentally. Without SOC their mode frequency depends on the trapping geometry and the ratio of the kinetic energy to the trapping energy. The results in the presence of spin–orbit coupling are shown in Fig. 10(a), where the experimental data points are overlaid on the results obtained from numerically solving the GP equation. Here the quadrupole period, $T_{\rm so}$, is scaled in units of the period T measured for the off-resonant case ($\delta \gg \Omega$). This allows one to remove the dependence on the trap geometry, which is slightly different for each Rabi frequency [see Figs. 10(b) and (c)]. The experimental and the numerical calculation both show that the peak of the quadrupole period lies around the critical point and that the oscillations show strong damping in the transition region. These behaviors are the same as for the dipole and the scissors oscillations.

In this section, we have summarized the recent results for the phase transition between the plane wave and conventional BEC phases in a weakly trapped BEC with SOC. The plane wave phase shows spin polarization and spontaneously occupies one of the two minima in momentum space. The conventional BEC phase is characterized by zero quasimomentum and spin balance. The phase transition between these two, which is of second order, has been confirmed both theoretically and experimentally to be of Dicke-type, using ground state variables as well as the properties of the collective excitations. The connections between SOC BECs and the Dicke model provides a new and powerful tool to theoretically and experimentally explore Dicke physics using a SOC BEC (such as recent studies about spin squeezing [113, 114]).

4 Homogeneous spin–orbit-coupled BEC: Bragg spectroscopy measurement of roton-like structures and Zitterbewegung

4.1 Bragg spectroscopy indicating roton-like excitation

Above, we study a weakly trapped case. Now, we consider a homogeneous BEC with experimentally realized SOC. We present our experimental measurements of collective excitations through standard Bragg spectroscopy, revealing the existence of a roton-like excitation [23].

In the literature, both ground states and collective excitations of homogeneous systems are discussed. With the use of a physically straightforward variational method, ground states are demonstrated to include plane wave, stripe, and conventional BEC phases [41, 43]. The full phase diagram can be labeled by various parameters,

such as δ, Ω, and the nonlinear coefficients g [41, 43, 115]. Once the ground states are known, their collective excitations can be analyzed using the standard Bogoliubov-de-Gennes (BdG) equations. It has been shown that the excitation spectrum of a plane wave phase features a roton-like structure [23, 115–117]. The stripe phase, which is a superfluid phase with a broken continuous translational symmetry due to density crystallinity, exhibits an excitation spectrum comprised of two linear phonon modes [47].

The roton-like structure of the plane wave phase can be understood in the following way. For a conventional BEC, the collective excitation spectrum is considered as an overall upwards displacement of the linear spectrum due to the mean-field repulsive interaction energy. At the same time, we consider the long wavelength regime, $|q| < 1/\xi$, where q is the quasimomentum of the excitation and ξ is the healing length. The excitation spectrum in this regime has a linear dispersion that generates phonon modes. The same intuitive picture is used for SOC BECs.

First, let us begin from a linear system with the Hamiltonian

$$H_{\rm soc} = -\frac{1}{2}\frac{\partial^2}{\partial x^2} - \mathrm{i}\frac{\partial}{\partial x}\sigma_z + \frac{\delta}{2}\sigma_z + \frac{\Omega}{2}\sigma_x. \tag{29}$$

The corresponding spectrum is characterized by a double well structure in momentum space as shown by the dotted line in Fig. 11(a). The collective excitation spectrum can be constructed by an upwards shift of the double well and the creation of a phonon mode in the long wavelength regime, as shown by the solid line in Fig. 11(a). Besides the well-known phonon mode, there is a clear parabolic minimum at finite quasimomentum in the excitation spectrum. Such a minimum is analogous to a roton excitation in the context of superfluid helium [118–121] and systems with long-range [122–125] (or finite-range [126, 127]) interactions. However, in this regime the minimum at finite momentum originates from the double well structure of the linear spectrum. For other parameter regimes, such as the regime of very large δ, no double well exists in the linear spectrum and such minima disappear accordingly. To distinguish this type of roton excitation from the one that could be found in systems with long-range interaction or in superfluid helium, we call the minimum a *roton-like* excitation.

We experimentally measure the roton-like excitation by performing Bragg spectroscopy [23]. This experimental technique has become a standard method for measuring the collective excitations of a BEC [128]. Since its first employment in BEC systems [129], Bragg spectroscopy has been used to reveal excitations in diverse situations, such as homogeneous BECs [131–133], BECs in optical lattices [134–137], and dipolar BECs [138].

Our experimental results are interpreted by theoretical analysis [23]. A BEC is described by the Gross–Pitaevskii (GP) equation,

$$H_{\rm soc}\Psi + H_{\rm int}\Psi = \mu\Psi, \tag{30}$$

where μ is the chemical potential, $H_{\rm soc}$ the linear Hamiltonian in Eq. (29), and $H_{\rm int}$ the nonlinear term described in Eq. (16). The general wave function $\Psi_{\uparrow,\downarrow}(x,t)$, is given by

$$\Psi_{\uparrow,\downarrow}(x,t) = \mathrm{e}^{-\mathrm{i}\mu t + \mathrm{i}kx}\left[\Phi_{\uparrow,\downarrow}(x,t) + \delta\Phi_{\uparrow,\downarrow}(x,t)\right], \tag{31}$$

where k, $\Phi_{\uparrow,\downarrow}$, and $\delta\Phi_{\uparrow,\downarrow}(x,t)$ are the momentum of the ground state, the ground state, and the perturbations of the system, respectively. These perturbations are given by

$$\begin{aligned}\delta\Phi_{\uparrow,\downarrow} = {} & U_{\uparrow,\downarrow}(x)\exp(\mathrm{i}qx - \mathrm{i}\delta\omega t) \\ & + V^*_{\uparrow,\downarrow}(x)\exp(-\mathrm{i}qx + \mathrm{i}\delta\omega^* t),\end{aligned} \tag{32}$$

where U, V are the two amplitudes, q is the quasimomentum, and $\delta\omega$ is the frequency of the perturbations. Substituting the general wave-function into the time-dependent GP equations, and keeping the terms U and V linear, we obtain the BdG equations,

$$\begin{pmatrix} H_\uparrow(k)+(q+k) & \frac{\Omega}{2}+g_{\uparrow\downarrow}\Phi_\uparrow\Phi^*_\downarrow & g_{\uparrow\uparrow}\Phi^2_\uparrow & g_{\uparrow\downarrow}\Phi_\uparrow\Phi_\downarrow \\ \frac{\Omega}{2}+g_{\uparrow\downarrow}\Phi^*_\uparrow\Phi_\downarrow & H_\downarrow(k)-(q+k) & g_{\uparrow\downarrow}\Phi_\uparrow\Phi_\downarrow & g_{\downarrow\downarrow}\Phi^2_\downarrow \\ -g_{\uparrow\uparrow}\Phi^{*2}_\uparrow & -g_{\uparrow\downarrow}\Phi^*_\uparrow\Phi^*_\downarrow & -H_\uparrow(-k)+(q-k) & -\left(\frac{\Omega}{2}+g_{\uparrow\downarrow}\Phi^*_\uparrow\Phi_\downarrow\right) \\ -g_{\uparrow\downarrow}\Phi^*_\uparrow\Phi^*_\downarrow & -g_{\downarrow\downarrow}\Phi^{*2}_\downarrow & -\left(\frac{\Omega}{2}+g_{\downarrow\downarrow}\Phi_\uparrow\Phi^*_\downarrow\right) & -H_\downarrow(-k)-(q-k) \end{pmatrix} \begin{pmatrix} U_\uparrow \\ U_\downarrow \\ V_\uparrow \\ V_\downarrow \end{pmatrix} = \delta\omega \begin{pmatrix} U_\uparrow \\ U_\downarrow \\ V_\uparrow \\ V_\downarrow \end{pmatrix}, \tag{33}$$

where $H_\uparrow(k) = -\mu + \frac{(q+k)^2}{2} + 2g|\Phi_\uparrow|^2 + g|\Phi_\downarrow|^2 + \frac{\delta}{2}$ and $H_\downarrow(k) = -\mu + \frac{(q+k)^2}{2} + g|\Phi_\uparrow|^2 + 2g|\Phi_\downarrow|^2 - \frac{\delta}{2}$. Note that all our GP and BdG equations are dimensionless. We use $2E_{\rm Ram} = (\hbar k_{\rm Ram})^2/m$ as the unit of energy. In this unit, the dimensionless SOC strength $\gamma = 1$.

The collective excitation spectrum $\delta\omega$ is calculated by

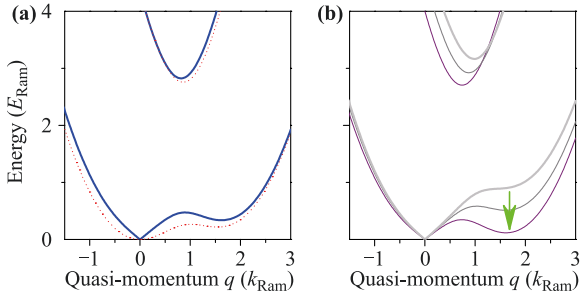

Fig. 11 **(a)** Single-particle dispersion (*red dotted line*) and BdG spectrum (*blue solid line*) of a SOC BEC for a nonlinear coefficient $g = 0.186$, Raman detuning $0.28E_{\rm Ram}$ ($\delta = 2\pi \times 500$ Hz), and Rabi frequency of $2.5E_{\rm Ram}$. **(b)** The roton-like mode softening with decreasing Raman detuning δ. The lines correspond to Raman detuning $1E_{\rm Ram}$, $0.5E_{\rm Ram}$, and 0 from top to bottom. Reproduced from Ref. [23].

diagonalizing the BdG equations. A typical result for a plane wave ground state in the case where $g_{\uparrow\uparrow} = g_{\downarrow\downarrow} = g_{\uparrow\downarrow}$ is shown by the solid line in Fig. 11(a). However, we find that when the Raman detuning δ is decreased, the roton-like structure softens as depicted in Fig. 11(b). The softening of the roton-like minimum becomes clearer when we consider miscible nonlinear coefficients (such as the ones in Fig. 12, $g_{\uparrow\uparrow} = g_{\downarrow\downarrow} \gg g_{\uparrow\downarrow}$). For a threshold value of the Raman detuning δ, the excitation energy becomes negative at the roton minimum (Fig. 12). Physically, a negative excitation means that the excited energy is smaller than the ground state energy. The excited state is thus energetically more preferable than the ground state, or, in other words, the ground state is energetically unstable. Therefore, the parameters for which the roton minimum touches zero establish a critical boundary. Beyond this boundary (corresponding to a much smaller Raman detuning), plane waves suffer an energetic instability. At that moment, the plane wave ground states cease to exist and the system enters into the stripe phase.

From the above study, we conclude that roton-like minimum softening is of great interest, because we are able to identify the phase transition between the plane wave phase and the stripe phase. In fact, roton softening is very important in the literature, because it becomes a possible route to generate a supersolid, an exotic phase of matter featuring superfluidity and density crystallinity at the same time. Interestingly, the stripe phase can also be understood as a kind of supersolid [47]. We would like to emphasize that, even though the roton-like minimum here is due to single particle physics, its softening relates to the supersolid phase transition, exactly correlating to true roton softening in long-range interactions and superfluid helium systems. Finally, we mention that the phase transition between the plane wave and stripe phases is of first order [43], just as for most other superfluid–supersolid transitions.

Because the roton-like minimum is an outstanding characteristic of the system, in our experiment we deliberately arrange the Bragg beams such that they probe the roton minimum. To perform Bragg spectroscopy, two counter-propagating Bragg laser beams are incident on the elongated SOC BEC. The Bragg beams are perturbative and drive transitions between the ground state and collective excitations. When tuned on resonance through the matching of momentum and energy imparted by the Bragg beams, the BEC becomes excited. The physical mechanism of Bragg spectroscopy is a two-photon resonance, schematically shown in Fig. 13(b). The momentum imparted by the Bragg beams is made equal to the momentum of an excitation at the position of the roton-like minimum [around $q = 1$ in Fig. 13(b)] by choosing appropriate parameters for the wavelength of the Bragg beams and the incident angle between them. Resonances

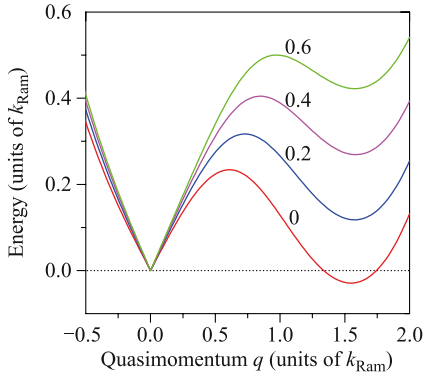

Fig. 12 Roton-like minimum softening and energetic instability for decreasing Raman detuning δ in a miscible regime ($g_{11} = g_{22} = 0.186, g_{12} = 0.08$) with $\Omega = 2.5E_{\rm Ram}$. The lines correspond to the Raman detuning of $0.6E_{\rm Ram}$, $0.4E_{\rm Ram}$, $0.2E_{\rm Ram}$ and 0 from top to bottom. Reproduced from Ref. [23].

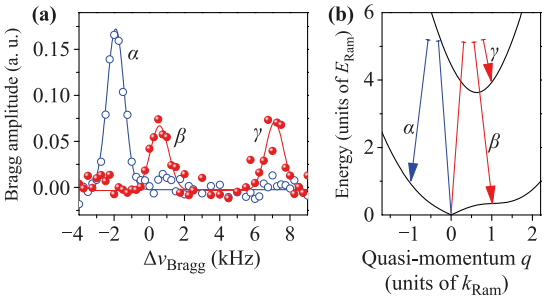

Fig. 13 **(a)** Bragg spectroscopy for a SOC BEC. $\hbar\Omega = 3.5E_{\rm Ram}$ and $\delta = 2\pi \times 500$ Hz. Each point is an average over four measurements. **(b)** Schematic description of the transitions corresponding to the three peaks in the spectrum. Reproduced from Ref. [23].

occur when tuning the frequency difference between the beams. As shown in Fig. 13(b), once the input momentum is fixed, there are three primary resonance conditions, labeled by α, β, and γ in Fig. 13(b). Two of the resonances (α and β) occur in the lower branch of the excitation spectrum, where one (β) is located at the roton-like minimum. The remaining resonance (γ) occurs in the higher branch. Another resonance should occur in the higher branch in the negative quasimomentum direction, but this resonance requires a large resonant energy. Because it is not relevant to the roton-like structure study, we do not consider this resonance. The Bragg spectroscopy signals are depicted in Fig. 13(a) by counting the number of atoms in the excited state. By fitting the position of each resonant peak, we obtain the excitation spectrum.

Roton-like mode-softening can be observed by varying the Raman detuning, δ. By repeating the process used to find the position of the resonant peaks in Fig. 13(a) for different values of the detuning, the data of Fig. 14(a) are obtained. One can easily see that the positions of the Bragg peaks are shifted as a function of δ; The roton-like mode (β) softens for decreasing positive values of the Raman detuning. Figure 14(b) is a zoomed-in plot of the roton-like mode softening. We note that the softening does not reach zero, and there is always a roton minimum gap [the lowest value shown in Fig. 14(b)]. This is because the experimental nonlinear coefficients are such that the system is in the very weakly miscible regime. The three coefficients are nearly equal ($g_{\uparrow\uparrow} \approx g_{\downarrow\downarrow} \approx g_{\uparrow\downarrow}$), which does not support the stripe phase as a ground state for experimentally convenient Raman laser powers. Therefore, regardless of the value of the Raman detuning, the ground state is always in the plane wave phase.

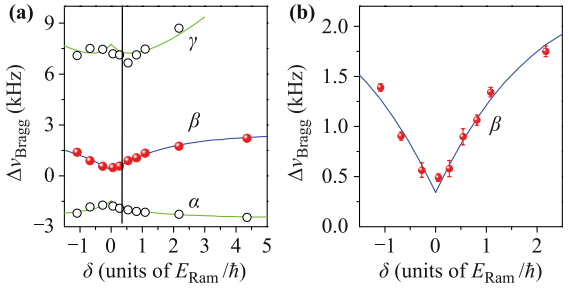

Fig. 14 **(a)** Location of Bragg peaks as a function of Raman detuning. Each point is an average over four data runs. These data were taken for $\hbar\Omega = 3.5E_{\mathrm{Ram}}$. The vertical error bars in (a) are approximately the symbol size. The data quality in the uppermost branch is impacted by the smallness of the spin overlap between the initial and final state. **(b)** Zoomed-in view of the data for peak β. The lines in (a) and (b) represent the result of theoretical calculations. Reproduced from Ref. [23].

The existence of the finite roton minimum gap prevents the system from transitioning from plane wave to stripe phases. Furthermore, we find that there is a symmetry between the data points for positive and negative detuning. The symmetry originates directly from the time-reversal-like symmetry of the Hamiltonian (29) and the GP equation (30), described by $\mathcal{R}_\delta K\sigma_x$, where $\mathcal{R}_\delta$ flips the sign of the detuning, $\mathcal{R}_\delta\delta\mathcal{R}_\delta^\dagger = -\delta$, and K is the complex conjugation operator. When the Raman detuning becomes negative, the shape of the dispersion relation of the Hamiltonian (29) changes such that the ground state of the BEC now has a quasimomentum opposite to the value at positive detuning.

Finally, we point out that during our experiments, two other groups performed Bragg spectroscopy measurements of roton-like structures in a BEC [29, 139]. Thus, Ref. [29] uses a system similar to ours and the roton-like minimum softening is observed by fixing the Raman detuning, δ, and varying the tuning of the Rabi frequency, Ω.

4.2 Collective dynamics: Zitterbewegung

The collective dynamics of homogeneous BECs with experimentally realizable SOC have been investigated in Refs. [140–145]. The unique and distinguished dynamical feature of these systems is the coupling between the spin dynamics and motional degrees of freedom (such as center-of-mass motion). The coupling between the spin dynamics and external degrees of freedom can be implemented in two different ways: the spin and momentum can be connected through SOC or by spin-dependent interactions. In the presence of SOC, spin dynamics directly affects the behavior of the momentum. In the presence of spin-dependent interactions, spin dynamics affects the interaction energy, subsequently leading to a change of the external dynamics such as the breathing mode [140]. In this section, we review our experiments investigating the coupling between the spin oscillation and an oscillation of external quantities such as velocity and position induced by a sudden quenching of the spin–orbit coupling parameters [21].

Our observations relate to Zitterbewegung (ZB), i.e., a rapidly trembling motion first predicted for a relativistic Dirac particle. It is one of the outstanding predictions from relativistic quantum mechanics due to Schrödinger [146]. In a Dirac system, ZB is generated by the interference of positive and negative energy states. The direct observation of ZB of real relativistic electrons is difficult because the amplitude of the trembling motion is extremely tiny and its frequency is extremely high [147]. However, such exotic motion has been simulated experimentally in different systems such as trapped ions [148], optical waveguide arrays [149] and BECs [17, 21]. The

motivation behind these experiments [17, 148, 149] is the preparation of the simplest Dirac system having one time and just one spatial dimension. Such a 1 + 1-dimensional Dirac system is described by a two-component spinor. The dispersion exhibits two branches. The gap between these two branches is related to the mass of the particle. Because the two bands are inverted relative to one another, the velocity of a particle with a given quasimomentum is opposite in the two branches. Therefore, Rabi oscillations between the two branches are accompanied by a velocity oscillation (furthermore leading to an oscillation of the particle's position), which is ZB. For the observation of the effect, it is not essential that the velocity of the particle is exactly opposite for the two branches. As described by the theoretical proposals of Refs. [150, 151], bands split by SOC demonstrate ZB as long as the two velocities are different. Furthermore, the particles do not need to be placed exactly at the position of the avoided crossing between the two dispersion bands to observe the motion.

In our experiments, we exploit the 1D SOC to simulate ZB [21]. We first prepare a SOC BEC as described in detail in the previous sections. The experimental scheme is shown in Figs. 15(a) and (b). Only two of the three ground states of ^{87}Rb atoms are coupled by Raman beams. We first prepare a BEC in the ground state of the lower spin–orbit band with a quasimomentum at the band minimum. Then, the collective dynamics is induced by a rapid jump in the Raman detuning δ [Fig. 15(c)] or the Rabi frequency Ω [Fig. 15(d)]. The quenching of the Raman detuning from δ to $-\delta$ can be implemented by a sudden jump in the frequency difference between the two Raman lasers, because a relative phase jump of π between the Raman lasers leads to a jump of the Rabi frequency from Ω to $-\Omega$. In the experiment, we record the mean velocity $\langle v_x \rangle$ of the atoms in the direction of the Raman coupling, which is defined as [21]

$$\langle v_x \rangle = \frac{\hbar}{m}(q + k_{\mathrm{Ram}} \langle \sigma_z \rangle) = \frac{N_\uparrow v_\uparrow + N_\downarrow v_\downarrow}{N}, \qquad (34)$$

where N is the total atom number and $N_\uparrow$ and $N_\downarrow$ are the number of atoms in the upper and lower component, respectively.

$$v_\uparrow = \hbar(q + k_{\mathrm{Ram}})/m, \quad v_\downarrow = \hbar(q - k_{\mathrm{Ram}})/m, \qquad (35)$$

are the velocities of the two components, where k_{Ram} is the magnitude of the wave vector of one Raman laser projected onto the x direction [Fig. 15(a)] and q the quasimomentum. Note that there is a $2\hbar k_{\mathrm{Ram}}/m$ velocity difference between the two components due to the laser momentum. From the first equality of Eq. (34), we can see that the spin oscillations of $\langle \sigma_z \rangle$ lead to oscillations in $\langle v_x \rangle$ and thus to ZB. We measure $N_{\uparrow,\downarrow}$ and the quasimomentum q for each time step after quenching the

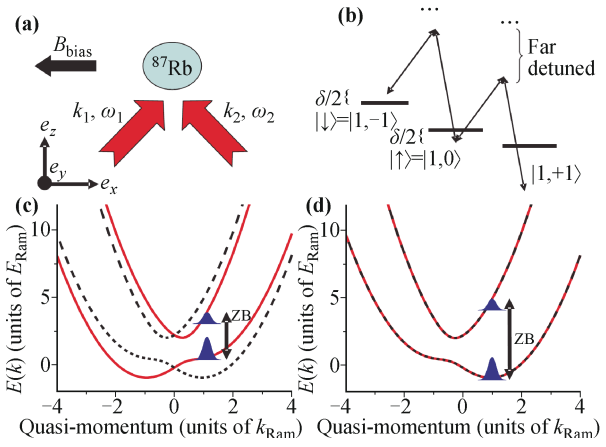

Fig. 15 **(a)** Experimental scheme for the creation of SOC. **(b)** The two-photon interaction between Raman lasers and the $F = 1$ manifold of a ^{87}Rb BEC. **(c)** Typical band structure before (*dashed-black*) and after (*solid-red*) quenching the system by changing the detuning from δ to $-\delta$. The wave packets symbolically show the wave function directly after the quench. The short time dynamics are dominated by ZB oscillations. **(d)** Similar to (c), but for a jump of the relative phase between the two Raman beams, i.e., quenching Ω to $-\Omega$. The band structure is unaltered by the phase jump. Reproduced from Ref. [21].

Raman parameters by performing time-of-flight imaging in the presence of a spin-resolving Stern–Gerlach field, which separates the two components. For the numerical analysis, we use the 2D GP equation in the presence of a weak harmonic trap to simulate the experimental cigar-shaped geometry. We first find the ground state through imaginary time evolution for fixed SOC parameters. The mean velocity $\langle v_x \rangle$ is then traced numerically after the quench.

Experimental and theoretical results obtained by quenching the detuning δ are shown in Fig. 16. Here $\Omega = 2.5E_{\mathrm{Ram}}$ and the initial detuning is $\delta = 6.25E_{\mathrm{Ram}}$. The detuning is then quenched to $\delta = -6.25E_{\mathrm{Ram}}$, where $E_{\mathrm{Ram}} = \hbar^2 k_{\mathrm{Ram}}^2/(2m)$ is the recoil energy. The dynamics after the quench features a rapid population oscillation between the two components. An experimental snapshot obtained by time-of-flight imaging is shown in Fig. 16(c). The time evolution of the mean velocity is shown in Fig. 16(a). Both the experimental data (open circles) and the results of a numerical calculation (solid line) indicate that the mean velocity oscillates perfectly for the first few periods. The measured and calculated quasimomenta are illustrated in the top of Fig. 16(a) by the filled black circles and the black line, respectively. On such short time scales, the quasimomentum is almost constant [i.e., $q = k_x$ in Fig. 16(c)]. The ZB frequency is determined by the energy splitting between the two SOC bands. For the parameters used in Fig. 16(a) the ZB fre-

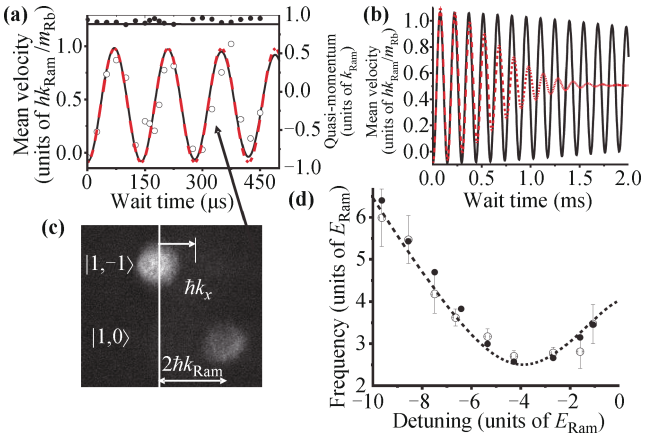

Fig. 16 **(a)** Experimental observation of the ZB oscillation of $\langle v_x\rangle$ for $\Omega = 2.5E_{\rm Ram}$ and δ quenched from $6.42E_{\rm Ram}$ to $-6.42E_{\rm Ram}$. Open circles are experimental data, the black line is from the numerical simulations of the GP equation, and the dashed red line is an analytical prediction from the single-particle Hamiltonian. Experimental (*black dot*) and numerical (*solid line*) quasimomenta are shown in the top part of the plot. **(b)** $\langle v_x\rangle$ for numerical simulation of the experimental parameters with [*solid line*, same as (a)] and without (*dashed line*) interactions. **(c)** Experimental image taken at $t = 325$ μs, showing the Stern–Gerlach separation and the $2\hbar k_{\rm Ram}$ photon momentum separation of the bare states. **(d)** Experimental (*open circles*) and numerical results (*filled circles*) for the ZB oscillation frequency vs. δ after the quench. The dashed line shows the band splitting calculated from the effective two band model for $\Omega = 2.5E_{\rm Ram}$. The experimental error bars are determined from fit uncertainties, shot-to-shot variations of k_x, and calibration uncertainty of Ω. Reproduced from Ref. [21].

quency is $3.62E_r$. The oscillation frequencies obtained for different values of δ are plotted in Fig. 16(d). The splitting between the spin–orbit bands without atomic interactions is $\Delta E = 2\sqrt{(\delta/2 + \hbar^2 q k_{\rm Ram}/m)^2 + (\Omega/2)^2}$, which is shown by the dotted line in Fig. 16(d). The agreement between the energy splitting and the measured oscillation frequency is very good.

After a few perfect oscillations, the ZB damps. Two mechanisms might be responsible for the experimentally observed damping: the finite momentum distribution of the initial BEC and the wave packet separation in real space. In a realistic experiment, the harmonic trap expands the momentum distribution of a BEC. The initial ground state has a finite momentum distribution around the minimum of the lower spin–orbit band, resulting in the ZB damping [151]. In contrast, the repulsive atomic interactions reduce the momentum distribution by expanding the wave function in the spatial domain. In this way, the many-body effects reduce the damping. Regarding the second damping mechanism, we note that the two spin–orbit bands have different group velocities. Thus, the wave packets of the two bands gradually separate in real space. The reduction of the overlap between the two wave packets then provides another ZB damping mechanism. After ZB has damped out, we observe dipole oscillation. The damping and subsequent dipole oscillation of the ZB are discussed in details in Ref. [21].

Similar ZB dynamics can also be triggered by quenching of the Rabi frequency Ω. We demonstrate this by quenching the Rabi frequency from Ω to $-\Omega$, see the short-time dynamics in Fig. 17(a). In this case, there is no change in the SOC band structure before and after the quench [Fig. 15(d)]. As an application, we can use such a quench to load a BEC into the upper SOC band. For this, two-phase jumps of the Raman lasers are implemented. We start with a BEC at the minimum of the lower spin–orbit band with $\Omega = 3.5E_{\rm Ram}$ and $\delta = 1.6E_{\rm Ram}$, where the majority of the population is $|\downarrow\rangle$. The first phase jump, changing Ω to $-\Omega$, triggers the ZB [Fig. 17(a)]. After half a period of the ZB, i.e., at $t_Z = 40$ μs, the atoms are in the upper band where the vast majority of the population is $|\uparrow\rangle$. We immediately apply the second phase jump that flips $-\Omega$ back to Ω. For the specific parameters used in this example, we load approximately 80% of the BEC into the upper band near $q = k_x$.

This technique provides a pathway to explore upper band dynamics. The time sequence of the experiment is shown in Fig. 17(b). After loading a BEC into the upper band, it is allowed to evolve for some time $t_W - t_Z$. The

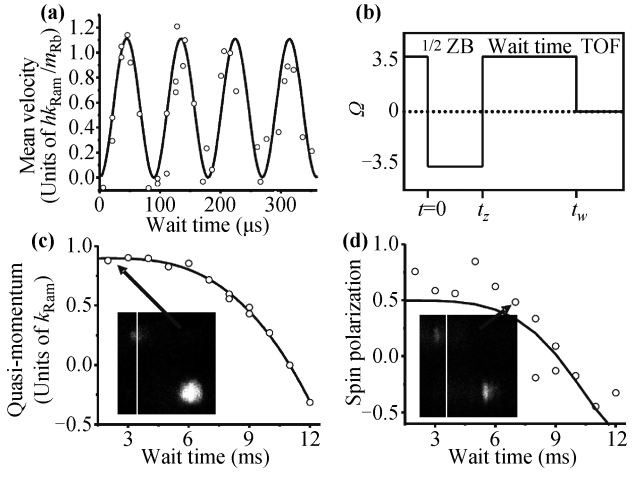

Fig. 17 Loading of the upper band via two-phase jumps separated by 40 μs where $\Omega = 3.5E_{\rm Ram}$ and $\delta = 1.6E_{\rm Ram}$. **(a)** Experimentally observed ZB oscillations (*open circles*) after a single-phase jump and the corresponding numerical simulations (*solid line*) of the experimental conditions. **(b)** The time sequence. **(c, d)** Experimentally observed quasimomentum and spin polarization, respectively. Insets are experimental images taken during the evolution, where the vertical line indicates zero kinetic momentum. Reproduced from Ref. [21].

quasimomentum [Fig. 17(c)] and spin polarization, defined as $(N_\uparrow - N_\uparrow)/(N_\uparrow + N_\uparrow)$, [Fig. 17(d)] are recorded for various evolution times. We see that the BEC moves toward the minimum of the upper band along the upper band dispersion [Fig. 15(d)]. For comparison, we calculate the expected single-particle dynamics for atoms in the upper band [plotted as lines in Figs.17(c) and (d)], based on the upper band dispersion relation. Both the predicted quasimomentum and spin polarization fit the experimental results very well, which indicates the single-particle nature of our observation.

In conclusion, quenching provides a flexible tool to manipulate SOC BECs. By quenching SOC parameters, rich dynamics is induced in the system. In our experiments, we have demonstrated how the physics of the ZB can be observed by quenching either the detuning or the Rabi frequency. Finally, we note that the investigation of the ZB has been generalized theoretically to spin-1 BECs with 2D SOC [153].

5 Spin–orbit-coupled lattice BEC: Flat bands and dynamical instability measurements

In this section, we review our work on BECs in an optical lattice with SOC [24, 104]. Optical lattices have already become one of most important experimental means to manipulate atoms, because we can have full experimental control of the system's initial conditions [154]. The combination of a periodic potential and SOC is particularly intriguing; many topological phenomena and exotic spin models can be constructed using this method (see Ref. [64] for a review). For example, in their classical paper [155], Kane and Mele studied intrinsic SOC in a honeycomb periodic potential and revealed the existence of the quantum spin Hall effect, opening an avenue to study topological insulator physics with a Z_2 index.

We now focus on nonlinear Bloch spectra and the corresponding nonlinear Bloch states in a SOC lattice BEC. It is well known that for a single-particle system with periodic potentials, Bloch's theorem applies. For a many-body BEC system, Bloch states are intriguing because they directly relate to the experimental preparation of the system. The stability of Bloch states is crucial to the superfluidity of a BEC [156].

5.1 Isolated flat bands

We have already described how SOC can change the spectrum of a homogeneous BEC (e.g., giving rise to a double-well spectrum). In optical lattices, we find that SOC also dramatically modifies the Bloch spectrum. The most outstanding feature concerns the lowest Bloch band, which may be flat [104, 157]. In the following discussion, we first provide an intuitive mechanism behind the existence of the flat band, and then demonstrate its properties.

The flat band may be understood in the following way. The spectrum of the SOC Hamiltonian is described by $H_0 = p_x^2/2 + \gamma p_x \sigma_z + \Omega \sigma_x$ and is characterized by two branches $\mu_\pm = k^2/2 \pm \sqrt{\gamma^2 k^2 + \Omega^2}$. In the lower branch, and for low values of the Rabi coupling strength Ω, there is a double-well structure as demonstrated in Fig. 18(a), with minima found at $k_{\min} = \pm\sqrt{\gamma^2 - \Omega^2/\gamma^2}$. The upper branch is found at an energy gap 2Ω at momentum $k = 0$. By increasing Ω, the energy gap also increases, appearing as though the Rabi frequency suppresses the central peak of the lower branch at $k = 0$.

In the presence of an optical lattice, the single-particle Hamiltonian becomes $H_0 + V_0 \sin^2 x$. The eigenvalues of this single-particle system form Bloch energy bands and a gap structure. We define the first Brillouin zone edges by the reciprocal lattice vectors, $k_{\text{edge}} = \pm 1$, which are represented by the vertical solid (blue) lines for $\gamma < 1$ and the vertical dashed (red) lines for $\gamma > 1$ in Fig. 18(a).

The mechanism for flat band generation is slightly different in two regimes $\gamma < 1$ and $\gamma \geq 1$. For $\gamma < 1$, at $\Omega = 0$, $|k_{\min}| = \gamma < |k_{\text{edge}}|$. At the edges of first Brillouin zone, energy gaps are opened to form the lowest Bloch band [see Fig. 18(b)]. The width of the lowest band is determined by the energy at the Brillouin zone edges measured relative to the energy at $k_{\min}$ [i.e., the value of h in Fig. 18(b)], and by the height of the central peak at $k = 0$. If γ is close to 1, indicating that the original band minima $k_{\min}$ are near the edges, the band edges become the lowest Bloch band minima, i.e., $h = 0$, and the band width only depends on the central peak height. By adiabatically increasing the Rabi coupling term Ω, the height of the central peak is gradually reduced. Therefore, the lowest band could become very flat for a specific region where the coupling is very strong. However, if γ is much smaller than 1, at $\Omega = 0$, the minima at $k_{\min}$ ap-

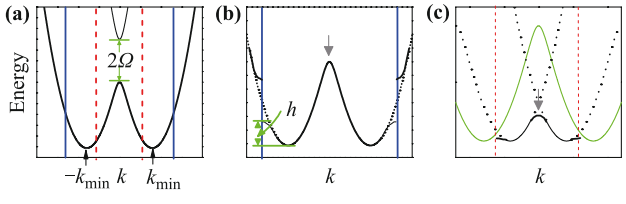

Fig. 18 Formation of isolated flat bands. **(a)** Energy spectrum $\mu_\pm(k)$ of a single particle Hamiltonian H_0. The vertical solid (or dashed) lines represent the possible location of the edges of the first Brillouin zone for $\gamma < 1$ ($\gamma > 1$). **(b)** Lowest Bloch band for $\gamma < 1$. The gray arrow describes the suppression of the central peak with increasing Ω. **(c)** Lowest Bloch band for $\gamma \geq 1$. The solid (green) line is $\mu_-(k)$, while the dotted lines are $\mu_-(k \pm 2)$. Reproduced from Ref. [104].

proach zero inside the first Brillouin zone and h will have a large energetic value. In this case, one cannot change the value of h by tuning Ω. Thus, the width of the lowest band cannot be squeezed flat.

In the other regime, $\gamma \geq 1$, the minima at $k_{\min}$ of H_0 are located outside of the first Brillouin zone [see Fig. 18(c)] at $\Omega = 0$. The lowest band is thus generated by folding the energy spectrum into the first Brillouin zone. This is done through shifting the energy spectrum of H_0 by a reciprocal lattice vector in momentum space. The band minima now are located at $k_{\min} \pm 2$, and then the physics is similar to the case $\gamma < 1$. Moreover, for $\gamma \geq 1$, the minima of the lowest band shift toward the band edges when Ω is adiabatically increased from 0. There is a specific range of Ω for which the band minimum remains at the band edge. In this region, a flat band can be realized where the central peak is suppressed with increasing Ω.

The above mechanism can be tested numerically, as demonstrated in Ref. [104]. To quantify the flatness of the lowest band, we define the ratio, R, as

$$R = \frac{\text{Band gap}}{\text{Width of the lowest band}}, \tag{36}$$

where the band gap describes the energy gap between the lowest and the first band at $k = 0$. Figures 19(a) and (b) show the ratio R for the case of $\gamma = 0.74 < 1$ and $\gamma = 1.05 > 1$, respectively, neglecting interatomic interactions (solid lines). Both cases indicate that for an appropriate Ω, the lowest Bloch band can be very flat in comparison with the gap between the lower two bands.

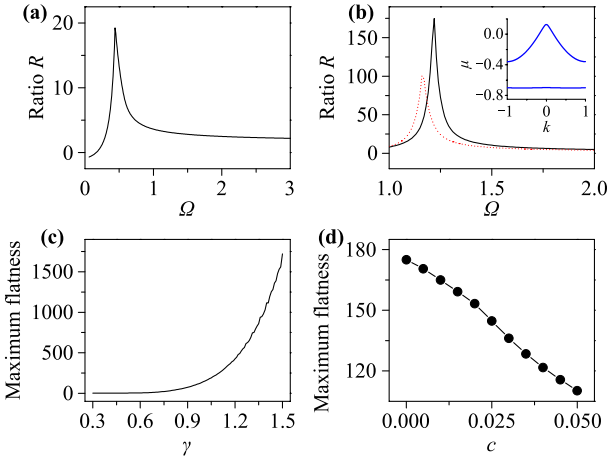

Fig. 19 Flatness (ratio R) of the lowest Bloch band. $V_0 = 1$. **(a)** $\gamma = 0.74$ and $c = 0$. **(b)** $\gamma = 1.05$. Solid line $c = 0$ and dashed line $c = 0.05$. In the inset, a typical example of a flat band is shown with $\Omega = 1.15, c = 0.05$. **(c)** The maximum flatness as a function of γ with $c = 0$. **(d)** The maximum flatness as a function of c with $\gamma = 1.05$. Reproduced from Ref. [104].

We note that the maximum flatness can reach 20 for $\gamma = 0.74$ and 170 for $\gamma = 1.05$. The suppression of the flatness for $\gamma = 0.74 < 1$ agrees with our intuitive physical mechanism: The band minima are far enough away from the first Brillouin zone edges that the lowest band cannot be squeezed to be exactly flat. The maximum flatness depends on the SOC strength, γ. With increasing γ, the lower band becomes flatter as shown in Fig. 19(c).

For a realistic BEC, the effects due to the nonlinear interactions between the atoms need to be taken into account. The numerical analysis should be based on the corresponding GP equation, $i\hbar\partial\Phi/\partial t = (H_0 + V_0 \sin^2 x)\Phi + c(|\Phi_\uparrow|^2 + |\Phi_\downarrow|^2))\Phi$. The nonlinearity, c, decreases the maximum flatness of the lower band but does not destroy it, as shown in Fig. 19(d). The maximum flatness with increasing nonlinearity is still very large. A typical nonlinear flat Bloch spectrum is shown in the inset plot of Fig. 19(b). For comparison, the dependence of the ratio R on Ω at $\gamma = 1.05$ is plotted for the nonlinear (dotted line) and linear (solid line) cases in Fig. 19(b).

5.2 Experimental measurement of dynamical instability using a translating optical lattice

One of the many interesting questions regarding a BEC in an optical lattice is the stability of the system [156]. Mathematically, the behavior of a BEC in a lattice is described by the nonlinear GP equation. A solution of a nonlinear equation may suffer from dynamical instabilities, i.e., perturbations to a solution can grow exponentially with time, resulting in the destruction of the solution. Another mechanism of instability can also destroy BEC: the energy instability. If the state of the system is not at a local minimum, the system will emit excitations to access the local minimum. Hence, the state is unstable. Both dynamical and energetic instabilities of a lattice BEC have been investigated extensively in theory [158–165] and experiment [166–168].

Theoretically, once a nonlinear Bloch wave is known, its stability can be analyzed by solving the BdG equations. Using this method, the stability of nonlinear Bloch waves at any quasimomentum k in an arbitrary band can be calculated [158–163, 165, 165]. In our experiments, the BEC is initially prepared in the ground state, which is located at the minimum of the lowest Bloch band. A moving optical lattice is then utilized to load a BEC effectively into its destined location in the band structure [167, 168]. Due to the Galilean invariance of a regular BEC, the physics of a moving optical lattice is equivalent to that of physically moving a BEC. However, for a SOC BEC, the Galilean invariance is broken, and these two schemes are no longer equivalent [44, 169]. Moreover, the results are expected to be asymmetric for lattices moving in different directions.

Motivated by the importance of stability and the lack of Galilean invariance, we experimentally observe the dynamical stability of a SOC BEC in a translating optical lattice [24]. We do not consider energetic instabilities because the time scale for an energetic instability is very long compared to that of a dynamical instability [167]. Furthermore, energetic instabilities require a dissipation of energy. In BEC experiments, this dissipation of energy can be introduced by a thermal atom cloud. The total trapping potential of the combined dipole trap and optical lattices is very shallow, providing an evaporative cooling mechanism that allows thermal atoms to escape from the trap. This prevents interactions between the BEC and the thermal atoms, thus negating any energy instabilities in the system.

In the following, we describe our theoretical analysis and experimental approach. A SOC ^{87}Rb BEC is prepared by the Raman dressing technique described in previous sections [see the experimental scheme shown in Figs. 20(a) and (b)]. The corresponding single-particle system is described by the Hamiltonian

$$H_{\rm soc} = \frac{p_x^2}{2m} + \gamma p_x \sigma_z + \frac{\hbar\delta}{2}\sigma_z + \frac{\hbar\Omega}{2}\sigma_x, \tag{37}$$

where SOC occurs in the x-direction with strength $\gamma = \hbar k_{\rm Ram}/m$, momentum $k_{\rm Ram} = 2\pi/(\lambda_{\rm Ram}\sqrt{2})$, and wavelength $\lambda_{\rm Ram}$, determined by the Raman beams. The energy spectrum of $H_{\rm soc}$ is $E_\pm(k_x) = \hbar^2 k_x^2/(2m) \pm \hbar\sqrt{(\gamma k_x + \delta/2)^2 + \Omega^2/4}$. A typical spectrum for our experimental parameters is depicted in Fig. 20(c).

The translating optical lattice is generated by two additional beams that are co-propagating with the Raman beams. The lattice velocity, $v = \pi\Delta\nu/k_{\rm lat}$, depends on the frequency difference $\Delta\nu$ between the two lattice beams, where $k_{\rm lat} = 2\pi/(\lambda_{\rm lat}\sqrt{2})$, and $\lambda_{\rm lat}$ is the wavelength of the lattice beams. The lattice intensity is ramped up adiabatically in the experiment, and the single-particle Hamiltonian of the SOC lattice system becomes

$$H_{\rm sp} = H_{\rm soc} + U_0 \sin^2[k_{\rm lat}(x - vt)]. \tag{38}$$

In our experiment, the optical lattice amplitude is then fixed at $U_0 = -1.4E_{\rm lat}$, where $E_{\rm lat} = \hbar^2 k_{\rm lat}^2/(2m)$.

Because the Hamiltonian $H_{\rm sp}$ is periodic, it features a Bloch spectrum. First, we consider a stationary lattice with $v = 0$. The spectrum for this case is shown in Fig. 20(d) and can be understood in the following way: We shift the SOC spectrum $E_\pm(k_x)$ by integer multiples of the reciprocal lattice vector $2n\hbar k_{\rm lat}$ in quasi-momentum, where $n = 0, \pm1, \pm2, \ldots$. Band gaps in the Bloch spectrum appear wherever the intersections between $E_\pm(k_x)$ and $E_\pm(k_x + 2nk_{\rm lat})$ occur.

Next, we consider a translating optical lattice with $v \neq 0$. In this case, the Hamiltonian $H_{\rm sp}$ is time dependent

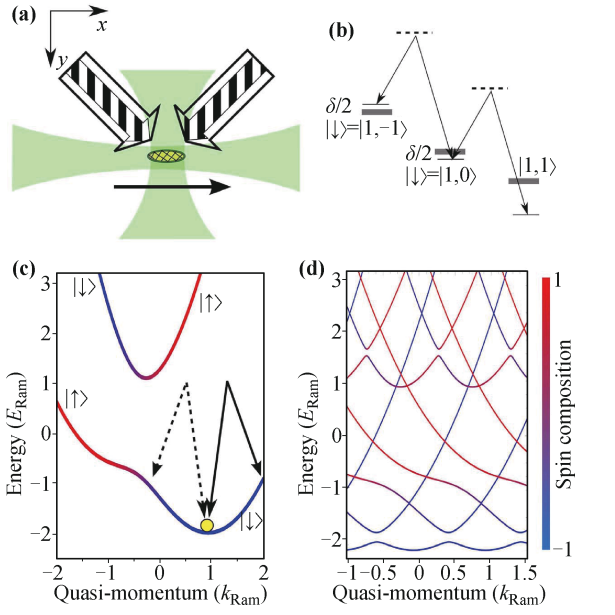

Fig. 20 **(a)** Experimental scheme. The BEC (*yellow hashed*) is confined in an optical dipole trap (*solid green*). Two sets of laser beams are optically aligned to intersect the BEC at a 45° angle for the generation of SOC (*white arrows*) and a translating optical lattice (*striped arrows*). **(b)** Raman coupling scheme in the $F = 1$ manifold of ^{87}Rb with detuning δ. **(c)** Typical band structure $E_\pm(k_x)$ of $H_{\rm SOC}$ with the color (*grey scale*) indicating the spin-polarization, defined as the relative population difference of the bare spin components $(|\psi_\uparrow|^2 - |\psi_\downarrow|^2)/(|\psi_\uparrow|^2 + |\psi_\downarrow|^2)$. The BEC is prepared at the minimum of the lower band (circle). The arrows indicate a possible two-photon coupling due to the lattice translating with negative (*dashed*) or positive (*solid*) velocity. **(d)** Bloch spectrum of a stationary optical lattice in the presence of spin–orbit coupling. The lines correspond to $E_\pm(k_x)$ and $E_\pm(k_x + 2nk_{\rm lat})$, where n is an integer. The spin composition is encoded in the line color (*grey scale*). The parameters used for (c) and (d) are $\hbar\delta = 1.6\ E_{\rm Ram}$, $\hbar\Omega = 2\ E_{\rm Ram}$ with the additional parameters $U_0 = -1.4E_{\rm lat}$ and $v = 0$ for (d). Reproduced from Ref. [24].

in the lab frame. It is then better to go into a co-moving frame where the optical lattice is stationary. This leads to the stationary Hamiltonian

$$H_{\rm sp}^M = \frac{p_x^2}{2m} + \gamma p_x \sigma_z + \frac{\hbar\delta}{2}\sigma_z + \frac{\hbar\Omega}{2}\sigma_x + U_0 \sin^2(k_{\rm lat}x) - vp_x \tag{39}$$

in the co-moving frame. After a substitution $P = p_x - mv$, one obtains $\bar{H}_{\rm sp}^M = \frac{P^2}{2m} + \gamma P\sigma_z + (\delta + 2m\gamma v/\hbar)\frac{\hbar}{2}\sigma_z + \frac{\hbar\Omega}{2}\sigma_x + U_0 \sin^2(k_{\rm lat}x)$, where a constant energy term $mv^2/2$ has been dropped. Comparing the SOC terms with the original $H_{\rm soc}$, we find that $\bar{H}_{\rm sp}^M$ is non-trivially different from $H_{\rm soc}$ due to the term $\delta + 2m\gamma v/\hbar$, which can be interpreted as an effective detuning of the Raman

beams. This term depends on the frame velocity v and signifies the broken Galilean invariance of the SOC BEC [44].

In the experiment, we observe the dynamical stability of the BEC as a function of the lattice velocity. After loading a SOC BEC into the translating lattice at a velocity v, the atoms are held for a variable time τ. For each τ, the atom number in the BEC is measured. In this way, we may get decaying behavior if the BEC is unstable. A loss rate, used to characterize the dynamical instability of the BEC, can be fitted to the measured decay. Experimental results of the loss rates measured as functions of lattice velocity are shown in the upper panel of each plot in Fig. 21. Each panel corresponds to a different Raman detuning δ. For a 1D translating lattice, there are two directions in which the lattice can move: negative (blue circles) and positive (red triangles).

The results indicate that for different moving directions of the lattice, the dynamical stability is quite different. This can be seen especially in the case of negative lattice motion. For example, for a large negative velocity there is an observable peak in the loss rate around $v = 9$ mm/s in Fig. 21(a), while there is no such peak for the positive direction. The location of this peak for the negative motion depends on the detuning; the peak shifts toward small velocities when the detuning is decreased (as seen in Fig. 21).

Furthermore, the critical velocity for the first onset of the instability at low velocities is also different for the two directions. This becomes much clearer for small values of δ. For example, in Fig. 21(d), the critical velocity is approximately 0.4 mm/s for the negative direction and 0.8 mm/s for the positive direction. The general conclusion of these experimental observations is as expected due to the lack of Galilean invariance: the loss rates for negative and positive lattice motions are not the same.

In the following, we present a detailed theoretical explanation of these experimental results. According to the experimental procedure, an effective dispersion relation should be developed as a function of the lattice velocity v. Initially, the BEC is prepared in the ground state of the SOC band $E_-(k_x)$ of $H_{\rm soc}$. Due to the SOC, the BEC in such a ground state has a finite quasimomentum, $k_{\rm min}$. When adiabatically ramping up the translating lattice

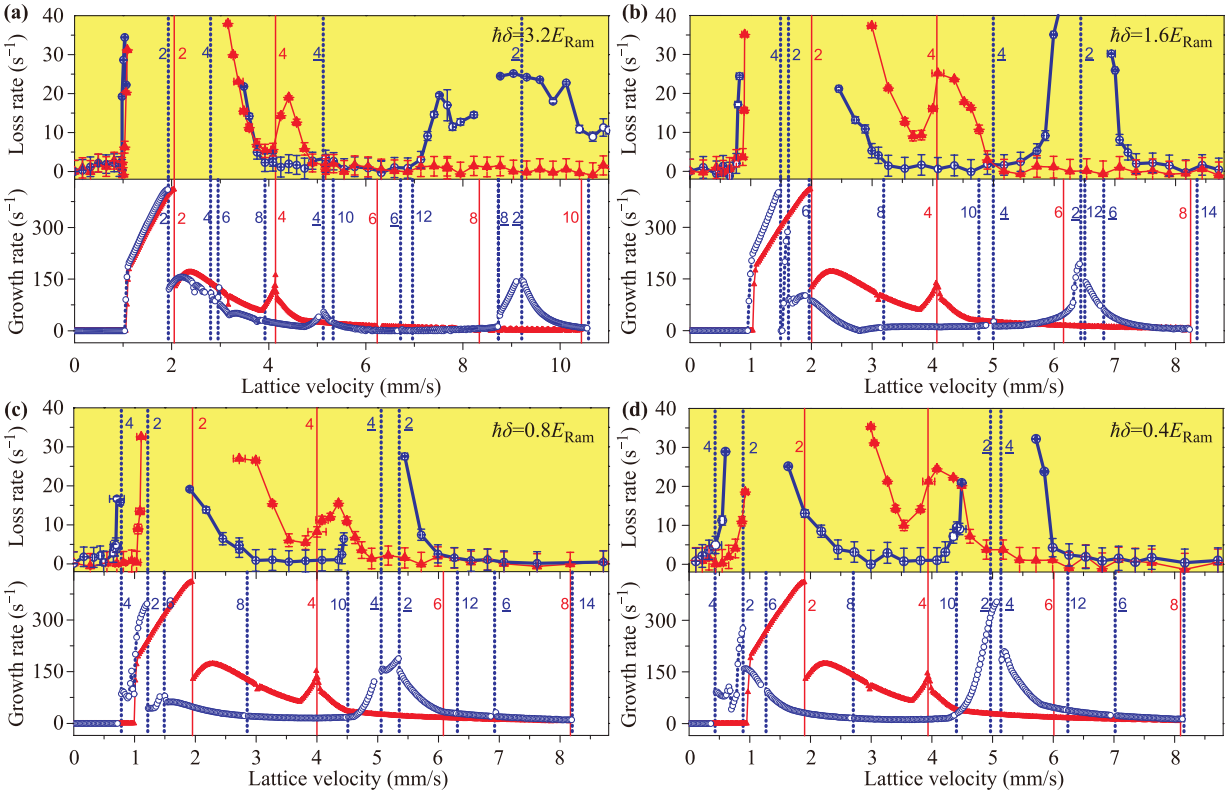

Fig. 21 Dynamical instability of the SOC BEC as a function of lattice velocity with **(a–d)** $\hbar\delta/E_{\rm Ram} = \{3.2, 1.6, 0.8, 0.4\}$, respectively. The strength of the dynamical instability is measured experimentally by the loss rate of atoms in the BEC (upper panels), while theoretically it is represented by the largest growth rate of the Bogoliubov excitations (lower panels). Each resonance (*vertical line*) is labeled with the number of photons generating the band edge, and where underlined integers denoting resonances between the upper and lower spin–orbit bands. The solid red triangles (*open blue circles*) indicate the positive (negative) direction of the lattice motion. Reproduced from Ref. [24].

intensity, the quasimomentum of the BEC is approximately conserved [170]. Therefore, we fix the quasimomentum to be $k_{\min}$ and the only remaining changeable parameter in $H_{\rm sp}^M$ is v.

The effective dispersion, $E^M(k_{\min}, v)$, can be taken from the Bloch spectrum of $H_{\rm sp}^M$ at $k_{\min}$. The results are shown in Fig. 22(a) for $\hbar\delta = 1.6\ E_{\rm Ram}$, $\hbar\Omega = 2\ E_{\rm Ram}$, and $U_0 = -1.4E_{\rm lat}$, where $E_{\rm Ram} = (\hbar k_{\rm Ram})^2/(2m)$. An obvious feature of the effective dispersion relation is its asymmetry with respect to a sign change of the lattice velocity. The physical origin of this asymmetry is in the breaking of Galilean invariance.

The thick green line in Fig. 22(a) shows the location in the effective band structure to which a BEC is loaded in the experiments by starting at the minimum of the lower SOC band and adiabatically ramping up the intensity of the moving lattice. To identify further the avoided crossings that a BEC may encounter for various lattice velocities, we label the avoided crossings by integers $2n$ according to the underlying multi-photon process. Underlined numbers $\underline{2n}$ are used to identify resonances occurring between the lower and upper spin–orbit bands. It is interesting to note that the ordering of the band gaps is not straightforward and that the positions of the band gaps are not equally spaced. The exact ordering and positions strongly depend on chosen parameters δ, Ω, and the ratio $k_{\rm lat}/k_{\rm Ram}$.

For comparison, Fig. 22(b) presents the analogous band structure for a BEC in a translating lattice without SOC. As is well known in this case, the effective band structure and BEC location (thick green line) are symmetric with respect to the direction of the motion, the band edges are equally spaced, and the effective dispersion relation recovers the well-known Bloch spectrum.

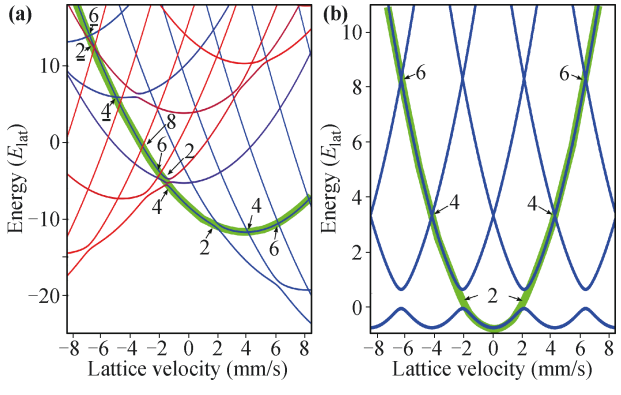

Fig. 22 Effective band structure as a function of the lattice velocity. The thick green lines indicate the position at which the BEC is placed in the experiments. **(a)** A BEC with SOC and $\hbar\delta = 1.6E_{\rm Ram}$ as shown in Fig. 21(b). **(b)** A BEC without SOC. The numbers in the graphs indicate the order of the associated multi-photon resonances. Reproduced from Ref. [24].

From the above theoretical analysis, we know the location of the BEC as a function of lattice velocity, i.e., we know which Bloch wave we should use for different lattice velocities. The Bloch spectrum and nonlinear Bloch wave are calculated by solving the 1D Gross–Pitaevskii equation in dimensionless form. Then, to model the experimental observation of the dynamical instability, we perform the BdG analysis. The detail Gross–Pitaevskii equations and BdG are presented in the supplementary material of Ref. [24]. The growth rate of excitations in the system is estimated as the largest imaginary value of any eigenvalues of the BdG equations, as this will dominate the growth. We use this growth rate to describe qualitatively the experimental loss rate measurement. The calculated results are shown in the lower panels of the plots in Fig. 21.

Through the digital numbers labeling the avoided crossings in Fig. 22(a), we know that the anomalous peak in Fig. 21(b) comes from the two-photon resonance $\underline{2}$ between $E_-^M(k_{\min}, v)$ and $E_+^M(k_{\min} - 2k_{\rm lat}, v)$ (i.e., the lattice resonance between the lower and upper spin–orbit bands). For comparison, the large loss feature near $v = 2$ mm/s is due to the 2-photon resonance within the lowest spin–orbit band. Even though both of these loss features arise from two-photon couplings, the $\underline{2}$ feature is weaker. This is in part due to the reduced overlap of the spin composition between $E_-^M(k_{\min}, v)$ and $E_+^M(k_{\min} - 2k_{\rm lat}, v)$.

In the positive direction of lattice motion, the $\underline{2}$ resonance occurs at $E_-^M(k_{\min}, v) = E_+^M(k_{\min} + 2k_{\rm lat}, v)$. This only happens at large velocities. For example, in the case of $\hbar\delta = 1.6\ E_{\rm Ram}$, such a resonance occurs at $v = 21.6$ mm/s. At such large velocities, the kinetic energy of a BEC completely dominates and the effect of the lattice is diminished. In this regime, the BEC behaves homogeneously. We know that for a homogeneous BEC, there is no dynamical instability. Thus, the anomalous peaks depicted in Fig. 21 are only observed for negative lattice motion and are not expected for positive lattice motion.

Finally, we comment that the dynamical instabilities are most significant near a band gap. This can be seen clearly in Fig. 21, where the peaks are outstanding at 2 and $\underline{2}$ photon resonance gaps. The dynamical instability of the system may thus be used as an experimental tool to calibrate the position of the band gaps.

In conclusion, we have studied both theoretically and experimentally the properties of the dynamical instabilities of a SOC BEC in a translating optical lattice. It is found that the instability depends on both the lattice velocity and the direction of motion, indicating a lack of Galilean invariance in the system. Finally, we note that a full ground state phase diagram in the SOC lattice BEC system was analyzed in a recent study [171].

We make one final comment. So far, we have discussed only 1D SOC. The 1D model is easily realized in experiments and is already exhibiting many exotic phenomena. However, in solid-state systems, the most common types of SOC are Rashba- and Dresselhaus-coupling, both of which typically are 2D. Compared to 1D SOC, the 2D case can exhibit topological properties (such as a nonzero Berry curvature and Chern number, Majorana fermions, etc.). This is in contrast to 1D SOC, which does not lead to topology. Motivated by the generation of topology and by the well-established studies of 2D SOC in condensed matter systems, there are strong theoretical [10, 172–176] and experimental efforts [30, 35, 36] in the cold atom community to prepare 2D SOC atomic systems. The phase diagram of a 2D SOC BEC possesses more features than the analogous 1D picture and the dynamics also differs, such as dipole oscillations [52].

6 Conclusion

In conclusion, we have reviewed our contributions to the theoretical and experimental advances in the field of SOC BECs and discussed some of the rich physics that can be found in this experimentally accessible system. The ground state of the system possesses three possible phases, depending on the SOC parameters. The transition between the plane wave phase and the conventional BEC phase is of Dicke-type type (and therefore a second order transition), which means that the system can be mapped to a Dicke model. Because SOC BECs are easy to access experimentally, they are, therefore, good candidates to explore other effects related to Dicke physics as well. The transition between the plane wave phase and the striped phase is a first order transition and can be investigated by looking at the collective excitations of the ground state in the plane wave phase. Here, the excitation spectrum features a roton-like minimum and its softening can be used to detect the phase transition point. Even though this roton-like structure stems from a single particle spin–orbit coupling effect, its softening relates deeply to the physics of supersolids. Hence, it can be used to understand this phenomenon. Our experimental measurements show the existence of these roton-like excitations by performing Bragg spectroscopy. Other collective excitations in a trapped case, such as quadruple oscillations, are also investigated to identify the phase transitions in the ground state. Furthermore, we have discussed the possibility that sudden quenching of the SOC parameters can lead to collective dynamics that can simulate the so-called Zitterbewegung, ZB, which is a well-known effect in relativistic physics. For a SOC BEC in an optical lattice, we have shown the existence of isolated flat bands in the lowest Bloch band and systematically investigated the dynamical stability, indicating the existence of a broken Galilean invariance in the system.

Acknowledgements We appreciate the collaborations with Chris Hamner, Chunlei Qu, M. Amin Khamehchi, Jiajia Chang, Ming Gong, Gang Chen, and Li Mao. Yongping Zhang and Thomas Busch were supported by Okinawa Institute of Science and Technology Graduate University. Peter Engels and Maren Elizabeth Mossman acknowledge funding from the National Science Foundation (NSF) through Grant No. PHY-1306662. Chuanwei Zhang was supported by ARO (W911NF-12-1-0334), AFOSR (FA9550-13-1-0045), and NSF (PHY-1505496).

References

1. A. L. Fetter, Rotating trapped Bose–Einstein condensates, *Rev. Mod. Phys.* 81(2), 647 (2009)
2. Y. J. Lin, R. L. Compton, K. Jiménez-García, J. V. Porto, and I. B. Spielman, Synthetic magnetic fields for ultracold neutral atoms, *Nature* 462(7273), 628 (2009)
3. M. Aidelsburger, M. Atala, M. Lohse, J. T. Barreiro, B. Paredes, and I. Bloch, Realization of the Hofstadter Hamiltonian with ultracold atoms in optical lattices, *Phys. Rev. Lett.* 111(18), 185301 (2013)
4. H. Miyake, G. A. Siviloglou, C. J. Kennedy, W. C. Burton, and W. Ketterle, Realizing the Harper Hamiltonian with laser-assisted tunneling in optical lattices, *Phys. Rev. Lett.* 111(18), 185302 (2013)
5. M. Aidelsburger, M. Atala, S. Nascimbène, S. Trotzky, Y.A. Chen, and I. Bloch, Experimental realization of strong effective magnetic fields in an optical lattice, *Phys. Rev. Lett.* 107(25), 255301 (2011)
6. I. Žutić, J. Fabian, and S. Das Sarma, Spintronics: Fundamentals and applications, *Rev. Mod. Phys.* 76(2), 323 (2004)
7. M. Z. Hasan and C. L. Kane, Colloquium: Topological insulators, *Rev. Mod. Phys.* 82(4), 3045 (2010)
8. T. Jungwirth, J. Wunderlich, and K. Olejník, Spin Hall effect devices, *Nat. Mater.* 11(5), 382 (2012)
9. Y. J. Lin, K. Jiménez-García, and I. B. Spielman, Spin–orbit-coupled Bose–Einstein condensates, *Nature* 471(7336), 83 (2011)
10. J. Ruseckas, G. Juzeliūnas, P. Öhberg, and M. Fleischhauer, Non-Abelian gauge potentials for ultracold atoms with degenerate dark states, *Phys. Rev. Lett.* 95(1), 010404 (2005)

11. S. L. Zhu, H. Fu, C. J. Wu, S. C. Zhang, and L. M. Duan, Spin Hall effects for cold atoms in a light-induced gauge potential, *Phys. Rev. Lett.* 97(24), 240401 (2006)
12. X. J. Liu, X. Liu, L. C. Kwek, and C. H. Oh, Optically induced spin-Hall effect in atoms, *Phys. Rev. Lett.* 98(2), 026602 (2007)
13. T. D. Stanescu, B. Anderson, and V. Galitski, Spin–orbit coupled Bose–Einstein condensates, *Phys. Rev. A* 78(2), 023616 (2008)
14. J. Larson, J. P. Martikainen, A. Collin, and E. Sjöqvist, Spin–orbit-coupled Bose–Einstein condensate in a tilted optical lattice, *Phys. Rev. A* 82(4), 043620 (2010)
15. M. Merkl, A. Jacob, F. E. Zimmer, P. Öhberg, and L. Santos, Chiral confinement in quasirelativistic Bose–Einstein condensates, *Phys. Rev. Lett.* 104(7), 073603 (2010)
16. R. A. Williams, L. J. LeBlanc, K. Jiménez-García, M. C. Beeler, A. R. Perry, W. D. Phillips, and I. B. Spielman, Synthetic partial waves in ultracold atomic collisions, *Science* 335(6066), 314 (2012)
17. L. J. LeBlanc, M. C. Beeler, K. Jiménez-García, A. R. Perry, S. Sugawa, R. A. Williams, and I. B. Spielman, Direct observation of Zitterbewegung in a Bose–Einstein condensate, *New J. Phys.* 15(7), 073011 (2013)
18. M. C. Beeler, R. A. Williams, K. Jiménez-García, L. J. LeBlanc, A. R. Perry, and I. B. Spielman, The spin Hall effect in a quantum gas, *Nature* 498(7453), 201 (2013)
19. K. Jiménez-García, L. J. LeBlanc, R. A. Williams, M. C. Beeler, C. Qu, M. Gong, C. Zhang, and I. B. Spielman, Tunable spin–orbit coupling via strong driving in ultracold-atom systems, *Phys. Rev. Lett.* 114(12), 125301 (2015)
20. L. W. Cheuk, A. T. Sommer, Z. Hadzibabic, T. Yefsah, W. S. Bakr, and M. W. Zwierlein, Spin-injection spectroscopy of a spin–orbit coupled Fermi gas, *Phys. Rev. Lett.* 109(9), 095302 (2012)
21. C. L. Qu, C. Hamner, M. Gong, C. W. Zhang, and P. Engels, Observation of Zitterbewegung in a spin–orbit coupled Bose–Einstein condensate, *Phys. Rev. A* 88, 021604(R) (2013)
22. C. Hamner, C. Qu, Y. Zhang, J. J. Chang, M. Gong, C. Zhang, and P. Engels, Dicke-type phase transition in a spin–orbit-coupled Bose–Einstein condensate, *Nat. Commun.* 5, 4023 (2014)
23. M. A. Khamehchi, Y. Zhang, C. Hamner, T. Busch, and P. Engels, Measurement of collective excitations in a spin–orbit-coupled Bose–Einstein condensate, *Phys. Rev. A* 90(6), 063624 (2014)
24. C. Hamner, Y. Zhang, M. A. Khamehchi, M. J. Davis, and P. Engels, Spin–orbit-coupled Bose–Einstein condensates in a one-dimensional optical lattice, *Phys. Rev. Lett.* 114(7), 070401 (2015)
25. A. J. Olson, S. J. Wang, R. J. Niffenegger, C. H. Li, C. H. Greene, and Y. P. Chen, Tunable Landau–Zener transitions in a spin–orbit-coupled Bose–Einstein condensate, *Phys. Rev. A* 90(1), 013616 (2014)
26. A. J. Olson, Chuan-Hsun Li, David B. Blasing, R. J. Niffenegger, and Yong P. Chen, Engineering an atom-interferometer with modulated light-induced 3π spin–orbit coupling, arXiv: 1502.04722 (2015)
27. J. Y. Zhang, S. C. Ji, Z. Chen, L. Zhang, Z. D. Du, B. Yan, G. S. Pan, B. Zhao, Y. J. Deng, H. Zhai, S. Chen, and J. W. Pan, Collective dipole oscillations of a spin–orbit coupled Bose–Einstein condensate, *Phys. Rev. Lett.* 109(11), 115301 (2012)
28. S. C. Ji, J. Y. Zhang, L. Zhang, Z. D. Du, W. Zheng, Y. J. Deng, H. Zhai, S. Chen, and J. W. Pan, Experimental determination of the finite-temperature phase diagram of a spin–orbit coupled Bose gas, *Nat. Phys.* 10(4), 314 (2014)
29. S. C. Ji, L. Zhang, X. T. Xu, Z. Wu, Y. Deng, S. Chen, and J. W. Pan, Softening of roton and phonon modes in a Bose-Einstein condensate with spin–orbit coupling, *Phys. Rev. Lett.* 114(10), 105301 (2015)
30. Z. Wu, L. Zhang, W. Sun, X. T. Xu, B. Z. Wang, S. C. Ji, Y. Deng, S. Chen, X. J. Liu, and J. W. Pan, Realization of two-dimensional spin–orbit coupling for Bose–Einstein condensates, arXiv: 1511.08170 (2015)
31. Z. K. Fu, P. J. Wang, S. J. Chai, L. H. Huang, and J. Zhang, Bose–Einstein condensate in a light-induced vector gauge potential using 1064-nm optical-dipole-trap lasers, *Phys. Rev. A* 84, 043609 (2011)
32. P. Wang, Z. Q. Yu, Z. Fu, J. Miao, L. Huang, S. Chai, H. Zhai, and J. Zhang, Spin–orbit coupled degenerate Fermi gases, *Phys. Rev. Lett.* 109(9), 095301 (2012)
33. Z. Fu, L. Huang, Z. Meng, P. Wang, X. J. Liu, H. Pu, H. Hu, and J. Zhang, Radio-frequency spectroscopy of a strongly interacting spin–orbit-coupled Fermi gas, *Phys. Rev. A* 87(5), 053619 (2013)
34. Z. Fu, L. Huang, Z. Meng, P. Wang, L. Zhang, S. Zhang, H. Zhai, P. Zhang, and J. Zhang, Production of Feshbach molecules induced by spin–orbit coupling in Fermi gases, *Nat. Phys.* 10(2), 110 (2013)
35. L. Huang, Z. Meng, P. Wang, P. Peng, S.L. Zhang, L. Chen, D. Li, Q. Zhou, and J. Zhang, Experimental realization of a two-dimensional synthetic spin–orbit coupling in ultracold Fermi gases, *Nat. Phys.* (2016), arXiv: 1506.02861
36. Z. Meng, L. Huang, P. Peng, D. Li, L. Chen, Y. Xu, C. Zhang, P. Wang, and J. Zhang, Experimental observation of topological band gap opening in ultracold Fermi gases with two-dimensional spin–orbit coupling, arXiv: 1511.08492 (2015)
37. X. Luo, L. Wu, J. Chen, Q. Guan, K. Gao, Z.F. Xu, L. You, and R. Wang, Tunable spin–orbit coupling synthesized with a modulating gradient magnetic field, *Sci. Rep.* 6, 18983 (2016), arXiv: 1502.07091
38. Y. Xu and C. Zhang, Topological Fulde–Ferrell superfluids of a spin–orbit coupled Fermi gas, *Int. J. Mod. Phys. B* 29(01), 1530001 (2015)

39. Y. Li, G. I. Martone, and S. Stringari, Bose-Einstein condensation with spin–orbit coupling, *Annual Review of Cold Atoms and Molecules* 3, 201 (2015)

40. C. Wang, C. Gao, C. M. Jian, and H. Zhai, Spin–orbit coupled spinor Bose–Einstein condensates, *Phys. Rev. Lett.* 105(16), 160403 (2010)

41. T. L. Ho and S. Zhang, Bose–Einstein condensates with spin–orbit interaction, *Phys. Rev. Lett.* 107(15), 150403 (2011)

42. C. J. Wu, I. Mondragon-Shem, and X. F. Zhou, Unconventional Bose–Einstein condensations from spin–orbit coupling, *Chin. Phys. Lett.* 28(9), 097102 (2011)

43. Y. Li, L. P. Pitaevskii, and S. Stringari, Quantum tricriticality and phase transitions in spin–orbit coupled Bose–Einstein condensates, *Phys. Rev. Lett.* 108(22), 225301 (2012)

44. Q. Zhu, C. Zhang, and B. Wu, Exotic superfluidity in spin–orbit coupled Bose–Einstein condensates, *Europhys. Lett.* 100(5), 50003 (2012)

45. L. Wen, Q. Sun, H. Q. Wang, A. C. Ji, and W. M. Liu, Ground state of spin-1 Bose–Einstein condensates with spin–orbit coupling in a Zeeman field, *Phys. Rev. A* 86, 043602 (2012)

46. X. L. Cui and Q. Zhou, Enhancement of condensate depletion due to spin–orbit coupling, *Phys. Rev. A* 87, 031604(R) (2013)

47. Y. Li, G. I. Martone, L. P. Pitaevskii, and S. Stringari, Superstripes and the excitation spectrum of a spin–orbit-coupled Bose–Einstein condensate, *Phys. Rev. Lett.* 110(23), 235302 (2013)

48. G. I. Martone, Y. Li, and S. Stringari, Approach for making visible and stable stripes in a spin–orbit-coupled Bose–Einstein superfluid, *Phys. Rev. A* 90, 041604(R) (2014)

49. Z. Lan and P. Öhberg, Raman-dressed spin-1 spin–orbit-coupled quantum gas, *Phys. Rev. A* 89, 023630 (2014)

50. S. Sinha, R. Nath, and L. Santos, Trapped two-dimensional condensates with synthetic spin–orbit coupling, *Phys. Rev. Lett.* 107(27), 270401 (2011)

51. H. Hu, B. Ramachandhran, H. Pu, and X. J. Liu, Spin–orbit coupled weakly interacting Bose–Einstein condensates in harmonic traps, *Phys. Rev. Lett.* 108(1), 010402 (2012)

52. Y. Zhang, L. Mao, and C. Zhang, Mean-field dynamics of spin–orbit coupled Bose–Einstein condensates, *Phys. Rev. Lett.* 108(3), 035302 (2012)

53. S. Gautam and S. K. Adhikari, Phase separation in a spin–orbit-coupled Bose–Einstein condensate, *Phys. Rev. A* 90(4), 043619 (2014)

54. O. V. Marchukov, A. G. Volosniev, D. V. Fedorov, A. S. Jensen, and N. T. Zinner, Statistical properties of spectra in harmonically trapped spin–orbit coupled systems, *J. Phys. At. Mol. Opt. Phys.* 47(19), 195303 (2014)

55. W. S. Cole, S. Zhang, A. Paramekanti, and N. Trivedi, Bose–Hubbard models with synthetic spin–orbit coupling: Mott insulators, spin textures, and superfluidity, *Phys. Rev. Lett.* 109(8), 085302 (2012)

56. Z. Cai, X. Zhou, and C. Wu, Magnetic phases of bosons with synthetic spin–orbit coupling in optical lattices, *Phys. Rev. A* 85, 061605(R) (2012)

57. M. J. Edmonds, J. Otterbach, R. G. Unanyan, M. Fleischhauer, M. Titov, and P. Öhberg, From Anderson to anomalous localization in cold atomic gases with effective spin–orbit coupling, *New J. Phys.* 14(7), 073056 (2012)

58. G. B. Zhu, Q. Sun, Y. Y. Zhang, K. S. Chan, W. M. Liu, and A. C. Ji, Spin-based effects and transport properties of a spin–orbit-coupled hexagonal optical lattice, *Phys. Rev. A* 88(2), 023608 (2013)

59. L. Zhou, H. Pu, and W. Zhang, Anderson localization of cold atomic gases with effective spin–orbit interaction in a quasiperiodic optical lattice, *Phys. Rev. A* 87(2), 023625 (2013)

60. Y. Qian, M. Gong, V. W. Scarola, and C. Zhang, Spin–orbit driven transitions between Mott insulators and finite momentum superfluids of bosons in optical lattices, arXiv: 1312.4011 (2013)

61. Y. V. Kartashov, V. V. Konotop, and F. K. Abdullaev, Gap solitons in a spin–orbit-coupled Bose–Einstein condensate, *Phys. Rev. Lett.* 111(6), 060402 (2013)

62. H. Sakaguchi and B. Li, Vortex lattice solutions to the Gross–Pitaevskii equation with spin–orbit coupling in optical lattices, *Phys. Rev. A* 87(1), 015602 (2013)

63. V. E. Lobanov, Y. V. Kartashov, and V. V. Konotop, Fundamental, multipole, and half-vortex gap solitons in spin–orbit coupled Bose–Einstein condensates, *Phys. Rev. Lett.* 112(18), 180403 (2014)

64. S. Zhang, W. S. Cole, A. Paramekanti, and N. Trivedi, Spin–orbit coupling in optical lattices, *Annual Review of Cold Atoms and Molecules* 3, 135 (2015)

65. D. Toniolo and J. Linder, Superfluidity breakdown and multiple roton gaps in spin–orbit-coupled Bose–Einstein condensates in an optical lattice, *Phys. Rev. A* 89, 061605(R) (2014)

66. J. Zhao, S. Hu, J. Chang, P. Zhang, and X. Wang, Ferromagnetism in a two-component Bose–Hubbard model with synthetic spin–orbit coupling, *Phys. Rev. A* 89(4), 043611 (2014)

67. Z. Xu, W. S. Cole, and S. Zhang, Mott-superfluid transition for spin–orbit-coupled bosons in one-dimensional optical lattices, *Phys. Rev. A* 89, 051604(R) (2014)

68. Y. Cheng, G. Tang, and S. K. Adhikari, Localization of a spin–orbit-coupled Bose–Einstein condensate in a bichromatic optical lattice, *Phys. Rev. A* 89(6), 063602 (2014)

69. M. Piraud, Z. Cai, I. P. McCulloch, and U. Schollwöck, Quantum magnetism of bosons with synthetic gauge fields in one-dimensional optical lattices: A density-matrix renormalization-group study, *Phys. Rev. A* 89(6), 063618 (2014)
70. W. Han, G. Juzeliūnas, W. Zhang, and W. M. Liu, Supersolid with nontrivial topological spin textures in spin–orbit-coupled Bose gases, *Phys. Rev. A* 91(1), 013607 (2015)
71. W. Li, L. Chen, Z. Chen, Y. Hu, Z. Zhang, and Z. Liang, Probing the flat band of optically trapped spin–orbital-coupled Bose gases using Bragg spectroscopy, *Phys. Rev. A* 91(2), 023629 (2015)
72. Y. Zhang, Y. Xu, and T. Busch, Gap solitons in spin–orbit-coupled Bose–Einstein condensates in optical lattices, *Phys. Rev. A* 91(4), 043629 (2015)
73. D. W. Zhang, L. B. Fu, Z. D. Wang, and S. L. Zhu, Josephson dynamics of a spin–orbit-coupled Bose–Einstein condensate in a double-well potential, *Phys. Rev. A* 85(4), 043609 (2012)
74. M. A. Garcia-March, G. Mazzarella, L. Dell'Anna, B. Juliá-Díaz, L. Salasnich, and A. Polls, Josephson physics of spin–orbit-coupled elongated Bose–Einstein condensates, *Phys. Rev. A* 89(6), 063607 (2014)
75. R. Citro and A. Naddeo, Spin–orbit coupled Bose–Einstein condensates in a double well, *Eur. Phys. J. Spec. Top.* 224(3), 503 (2015)
76. X. Q. Xu and J. H. Han, Spin–orbit coupled Bose–Einstein condensate under rotation, *Phys. Rev. Lett.* 107(20), 200401 (2011)
77. J. Radić T. A. Sedrakyan, I. B. Spielman, and V. Galitski, Vortices in spin–orbit-coupled Bose–Einstein condensates, *Phys. Rev. A* 84(6), 063604 (2011)
78. X. F. Zhou, J. Zhou, and C. Wu, Vortex structures of rotating spin–orbit-coupled Bose–Einstein condensates, *Phys. Rev. A* 84(6), 063624 (2011)
79. B. Ramachandhran, B. Opanchuk, X.J. Liu, H. Pu, P. D. Drummond, and H. Hu, Half-quantum vortex state in a spin–orbit-coupled Bose–Einstein condensate, *Phys. Rev. A* 85(2), 023606 (2012)
80. Y. X. Du, H. Yan, D. W. Zhang, C. J. Shan, and S. L. Zhu, Proposal for a rotation-sensing interferometer with spin–orbit-coupled atoms, *Phys. Rev. A* 85(4), 043619 (2012)
81. C.-F. Liu, H. Fan, Y.-C. Zhang, D.-S. Wang, and W.-M. Liu, Circular-hyperbolic skyrmion in rotating pseudo-spin-1/2 Bose–Einstein condensates with spin–orbit coupling, *Phys. Rev. A* 86, 053616 (2012)
82. L. Dong, L. Zhou, B. Wu, B. Ramachandhran, and H. Pu, Cavity-assisted dynamical spin–orbit coupling in cold atoms, *Phys. Rev. A* 89, 011602(R) (2014)
83. F. Mivehvar and D. L. Feder, Synthetic spin–orbit interactions and magnetic fields in ring-cavity QED, *Phys. Rev. A* 89(1), 013803 (2014)
84. Y. Deng, J. Cheng, H. Jing, and S. Yi, Bose–Einstein condensates with cavity-mediated spin–orbit coupling, *Phys. Rev. Lett.* 112(14), 143007 (2014)
85. B. Padhi and S. Ghosh, Spin–orbit-coupled Bose–Einstein condensates in a cavity: Route to magnetic phases through cavity transmission, *Phys. Rev. A* 90(2), 023627 (2014)
86. F. Mivehvar and D. L. Feder, Enhanced stripe phases in spin–orbit-coupled Bose–Einstein condensates in ring cavities, *Phys. Rev. A* 92(2), 023611 (2015)
87. Y. Deng, J. Cheng, H. Jing, C. P. Sun, and S. Yi, Spin–orbit-coupled dipolar Bose–Einstein condensates, *Phys. Rev. Lett.* 108(12), 125301 (2012)
88. R. M. Wilson, B. M. Anderson, and C. W. Clark, Meron ground state of Rashba spin–orbit-coupled dipolar bosons, *Phys. Rev. Lett.* 111(18), 185303 (2013)
89. S. Gopalakrishnan, I. Martin, and E. A. Demler, Quantum quasicrystals of spin–orbit-coupled dipolar bosons, *Phys. Rev. Lett.* 111(18), 185304 (2013)
90. H. T. Ng, Topological phases in spin–orbit-coupled dipolar lattice bosons, *Phys. Rev. A* 90(5), 053625 (2014)
91. Y. Yousefi, E. Ö. Karabulut, F. Malet, J. Cremon, and S. M. Reimann, Wigner-localized states in spin–orbit-coupled bosonic ultracold atoms with dipolar interaction, *Eur. Phys. J. Spec. Top.* 224(3), 545 (2015)
92. Y. Xu, Y. Zhang, and C. Zhang, Bright solitons in a two-dimensional spin–orbit-coupled dipolar Bose–Einstein condensate, *Phys. Rev. A* 92(1), 013633 (2015)
93. M. Gong, S. Tewari, and C. Zhang, BCS–BEC crossover and topological phase transition in 3D spin–orbit coupled degenerate Fermi gases, *Phys. Rev. Lett.* 107, 195303 (2011)
94. H. Hu, L. Jiang, X. J. Liu, and H. Pu, Probing anisotropic superfluidity in atomic Fermi gases with Rashba spin–orbit coupling, *Phys. Rev. Lett.* 107(19), 195304 (2011)
95. Z. Q. Yu and H. Zhai, Spin–orbit coupled Fermi gases across a Feshbach resonance, *Phys. Rev. Lett.* 107(19), 195305 (2011)
96. J. Dalibard, F. Gerbier, G. Juzeliūnas, and P. Öhberg, Colloquium: Artificial gauge potentials for neutral atoms, *Rev. Mod. Phys.* 83(4), 1523 (2011)
97. V. Galitski and I. B. Spielman, Spin–orbit coupling in quantum gases, *Nature* 494(7435), 49 (2013)
98. X. Zhou, Y. Li, Z. Cai, and C. Wu, Unconventional states of bosons with the synthetic spin–orbit coupling, *J. Phys. At. Mol. Opt. Phys.* 46(13), 134001 (2013)
99. N. Goldman, G. Juzeliūnas, P. Öhberg, and I. B. Spielman, Light-induced gauge fields for ultracold atoms, *Rep. Prog. Phys.* 77(12), 126401 (2014)
100. H. Zhai, Degenerate quantum gases with spin–orbit coupling: A review, *Rep. Prog. Phys.* 78(2), 026001 (2015)
101. P. J. Wang and J. Zhang, Spin-orbit coupling in Bose–Einstein condensate and degenerate Fermi gases, *Front. Phys.* 9(5), 598 (2014)

102. J. Zhang, H. Hu, X. J. Liu, and H. Pu, Fermi gases with synthetic spin–orbit coupling, *Annual Review of Cold Atoms and Molecules* 2, 81 (2014)

103. Y. Zhang, G. Chen, and C. Zhang, Tunable spin–orbit coupling and quantum phase transition in a trapped Bose–Einstein condensate, *Sci. Rep.* 3, 1937 (2013)

104. Y. Zhang and C. Zhang, Bose–Einstein condensates in spin–orbit-coupled optical lattices: Flat bands and superfluidity, *Phys. Rev. A* 87(2), 023611 (2013)

105. R. H. Dicke, Coherence in spontaneous radiation processes, *Phys. Rev.* 93(1), 99 (1954)

106. C. Emary, and T. Brandes, Chaos and the quantum phase transition in the Dicke model, *Phys. Rev. E* 67(6), 066203 (2003)

107. M. Gross and S. Haroche, Superradiance: An essay on the theory of collective spontaneous emission, *Phys. Rep.* 93(5), 301 (1982)

108. K. Baumann, C. Guerlin, F. Brennecke, and T. Esslinger, Dicke quantum phase transition with a superfluid gas in an optical cavity, *Nature* 464(7293), 1301 (2010)

109. Y. Li, G. Martone, and S. Stringari, Sum rules, dipole oscillation and spin polarizability of a spin–orbit coupled quantum gas, *Europhys. Lett.* 99(5), 56008 (2012)

110. S. Stringari, Collective excitations of a trapped Bose-condensed gas, *Phys. Rev. Lett.* 77(12), 2360 (1996)

111. D. Guéry-Odelin and S. Stringari, Scissors mode and superfluidity of a trapped Bose–Einstein condensed gas, *Phys. Rev. Lett.* 83(22), 4452 (1999)

112. O. M. Maragò, S. A. Hopkins, J. Arlt, E. Hodby, G. Hechenblaikner, and C. J. Foot, Observation of the Scissors mode and evidence for superfluidity of a trapped Bose–Einstein condensed gas, *Phys. Rev. Lett.* 84(10), 2056 (2000)

113. J. Lian, L. Yu, J. Q. Liang, G. Chen, and S. Jia, Orbit-induced spin squeezing in a spin–orbit coupled Bose–Einstein condensate, *Sci. Rep.* 3, 3166 (2013)

114. Y. Huang and Z. D. Hu, Spin and field squeezing in a spin–orbit coupled Bose–Einstein condensate, *Sci. Rep.* 5, 8006 (2015)

115. W. Zheng, Z. Q. Yu, X. Cui, and H. Zhai, Properties of Bose gases with the Raman-induced spin–orbit coupling, *J. Phys. At. Mol. Opt. Phys.* 46(13), 134007 (2013)

116. J. Higbie and D. M. Stamper-Kurn, Periodically dressed Bose–Einstein condensate: A superfluid with an anisotropic and variable critical velocity, *Phys. Rev. Lett.* 88(9), 090401 (2002)

117. G. I. Martone, Y. Li, L. P. Pitaevskii, and S. Stringari, Anisotropic dynamics of a spin–orbit-coupled Bose–Einstein condensate, *Phys. Rev. A* 86(6), 063621 (2012)

118. L. D. Landau, The theory of superfluidity of Helium II, *J. Phys. (USSR)* 5, 71 (1941)

119. H. Palevsky, K. Otnes, and K. E. Larsson, Excitation of rotons in Helium II by cold neutrons, *Phys. Rev.* 112(1), 11 (1958)

120. J. L. Yarnell, G. P. Arnold, P. J. Bendt, and E. C. Kerr, Excitations in liquid Helium: Neutron scattering measurements, *Phys. Rev.* 113(6), 1379 (1959)

121. D. G. Henshaw and A. D. B. Woods, Modes of atomic motions in liquid helium by inelastic scattering of neutrons, *Phys. Rev.* 121(5), 1266 (1961)

122. L. Santos, G. V. Shlyapnikov, and M. Lewenstein, Roton–Maxon spectrum and stability of trapped dipolar Bose–Einstein condensates, *Phys. Rev. Lett.* 90(25), 250403 (2003)

123. D. H. J. O'Dell, S. Giovanazzi, and G. Kurizki, Rotons in gaseous Bose–Einstein condensates irradiated by a laser, *Phys. Rev. Lett.* 90(11), 110402 (2003)

124. P. B. Blakie, D. Baillie, and R. N. Bisset, Roton spectroscopy in a harmonically trapped dipolar Bose–Einstein condensate, *Phys. Rev. A* 86(2), 021604 (2012)

125. M. Jona-Lasinio, K. Lakomy, and L. Santos, Time-of-flight roton spectroscopy in dipolar Bose–Einstein condensates, *Phys. Rev. A* 88(2), 025603 (2013)

126. Y. Pomeau and S. Rica, Model of superflow with rotons, *Phys. Rev. Lett.* 71(2), 247 (1993)

127. Y. Pomeau and S. Rica, Dynamics of a model of supersolid, *Phys. Rev. Lett.* 72(15), 2426 (1994)

128. R. Ozeri, N. Katz, J. Steinhauer, and N. Davidson, Colloquium: Bulk Bogoliubov excitations in a Bose–Einstein condensate, *Rev. Mod. Phys.* 77(1), 187 (2005)

129. J. Stenger, S. Inouye, A. P. Chikkatur, D. M. Stamper-Kurn, D. E. Pritchard, and W. Ketterle, Bragg spectroscopy of a Bose–Einstein condensate, *Phys. Rev. Lett.* 82(23), 4569 (1999)

130. D. M. Stamper-Kurn, A. P. Chikkatur, A. Görlitz, S. Inouye, S. Gupta, D. E. Pritchard, and W. Ketterle, Excitation of phonons in a Bose–Einstein condensate by light scattering, *Phys. Rev. Lett.* 83(15), 2876 (1999)

131. J. Steinhauer, R. Ozeri, N. Katz, and N. Davidson, Excitation spectrum of a Bose–Einstein condensate, *Phys. Rev. Lett.* 88(12), 120407 (2002)

132. J. Steinhauer, N. Katz, R. Ozeri, N. Davidson, C. Tozzo, and F. Dalfovo, Bragg spectroscopy of the Multibranch–Bogoliubov spectrum of elongated Bose–Einstein condensates, *Phys. Rev. Lett.* 90(6), 060404 (2003)

133. S. B. Papp, J. M. Pino, R. J. Wild, S. Ronen, C. E. Wieman, D. S. Jin, and E. A. Cornell, Bragg spectroscopy of a strongly interacting Rb^{85} Bose–Einstein condensate, *Phys. Rev. Lett.* 101, 135301 (2008)

134. X. Du, S. Wan, E. Yesilada, C. Ryu, D. J. Heinzen, Z. Liang, and B. Wu, Bragg spectroscopy of a superfluid Bose–Hubbard gas, *New J. Phys.* 12(8), 083025 (2010)

135. N. Fabbri, D. Clément, L. Fallani, C. Fort, M. Modugno, K. M. R. van der Stam, and M. Inguscio, Excitations of Bose–Einstein condensates in a one-dimensional periodic potential, *Phys. Rev. A* 79(4), 043623 (2009)

136. D. Clément, N. Fabbri, L. Fallani, C. Fort, and M. Inguscio, Exploring correlated 1D Bose gases from the superfluid to the Mott-insulator state by inelastic light scattering, *Phys. Rev. Lett.* 102, 155301 (2009)

137. P. T. Ernst, S. Götze, J. S. Krauser, K. Pyka, D. S. Lühmann, D. Pfannkuche, and K. Sengstock, Probing superfluids in optical lattices by momentum-resolved Bragg spectroscopy, *Nat. Phys.* 6(1), 56 (2010)

138. G. Bismut, B. Laburthe-Tolra, E. Maréchal, P. Pedri, O. Gorceix, and L. Vernac, Anisotropic excitation spectrum of a dipolar quantum Bose gas, *Phys. Rev. Lett.* 109(15), 155302 (2012)

139. L. C. Ha, L. W. Clark, C. V. Parker, B. M. Anderson, and C. Chin, Roton-Maxon excitation spectrum of Bose condensates in a shaken optical lattice, *Phys. Rev. Lett.* 114(5), 055301 (2015)

140. Z. Chen and H.Zhai, Collective-mode dynamics in a spin–orbit coupled Bose–Einstein condensate, *Phys. Rev. A* 86, 041604(R) (2012)

141. V. Achilleos, D. J. Frantzeskakis, and P. G. Kevrekidis, Beating dark–dark solitons and *Zitterbewegung* in spin–orbit-coupled Bose–Einstein condensates, *Phys. Rev. A* 89(3), 033636 (2014)

142. Sh. Mardonov, M. Palmero, M. Modugno, E. Ya. Sherman, and J. G. Muga, Interference of spin–orbit-coupled Bose–Einstein condensates, *Europhys. Lett.* 106(6), 60004 (2014)

143. Y. Li, C. Qu, Y. Zhang, and C. Zhang, Dynamical spin-density waves in a spin–orbit-coupled Bose–Einstein condensate, *Phys. Rev. A* 92(1), 013635 (2015)

144. Sh. Mardonov, E. Ya. Sherman, J. G. Muga, H. W. Wang, Y. Ban, and X. Chen, Collapse of spin–orbit-coupled Bose–Einstein condensates, *Phys. Rev. A* 91(4), 043604 (2015)

145. S. Cao, C. J. Shan, D. W. Zhang, X. Qin, and J. Xu, Dynamical generation of dark solitons in spin–orbit-coupled Bose–Einstein condensates, *J. Opt. Soc. Am. B* 32(2), 201 (2015)

146. E. Schrödinger, Über die kräftefreie Bewegung in der relativistischen Quantenmechanik, *Sitzungsber. Preuss. Akad. Wiss. Phys.-Math. Kl.* 24, 418 (1930)

147. W. Zawadzki and T. M. Rusin, Zitterbewegung (trembling motion) of electrons in semiconductors: A review, *J. Phys.: Condens. Matter* 23(14), 143201 (2011)

148. R. Gerritsma, G. Kirchmair, F. Zähringer, E. Solano, R. Blatt, and C. F. Roos, Quantum simulation of the Dirac equation, *Nature* 463(7277), 68 (2010)

149. F. Dreisow, M. Heinrich, R. Keil, A. Tünnermann, S. Nolte, S. Longhi, and A. Szameit, Classical simulation of relativistic Zitterbewegung in photonic lattices, *Phys. Rev. Lett.* 105, 143902 (2010)

150. J. Schliemann, D. Loss, and R. M. Westervelt, Zitterbewegung of electronic wave packets in III-V zinc-blende semiconductor quantum wells, *Phys. Rev. Lett.* 94, 206801 (2005)

151. J. Vaishnav and C. Clark, Observing Zitterbewegung with ultracold atoms, *Phys. Rev. Lett.* 100(15), 153002 (2008)

152. Y. J. Lin, R. L. Compton, K. Jiménez-García, W. D. Phillips, J. V. Porto, and I. B. Spielman, A synthetic electric force acting on neutral atoms, *Nat. Phys.* 7(7), 531 (2011)

153. Y.-C. Zhang, S.-W.Song, C.-F. Liu, and W.-M. Liu, Zitterbewegung effect in spin–orbit-coupled spin-1 ultracold atoms, *Phys. Rev. A* 87, 023612 (2013)

154. O. Morsch and M. Oberthaler, Dynamics of Bose–Einstein condensates in optical lattices, *Rev. Mod. Phys.* 78, 179 (2006)

155. C. L. Kane and E. J. Mele, Quantum spin Hall effect in graphene, *Phys. Rev. Lett.* 95(22), 226801 (2005)

156. Q. Zhu and B. Wu, Superfluidity of Bose–Einstein condensates in ultracold atomic gases, *Chin. Phys. B* 24(5), 050507 (2015)

157. F. Lin, C. Zhang, and V. W. Scarola, Emergent kinetics and fractionalized charge in 1D spin–orbit coupled Flatband optical lattices, *Phys. Rev. Lett.* 112, 110404 (2014)

158. Biao Wu and Qian Niu, Landau and dynamical instabilities of the superflow of Bose–Einstein condensates in optical lattices, *Phys. Rev. A* 64, 061603(R) (2001)

159. A. Smerzi, A. Trombettoni, P. G. Kevrekidis, and A. R. Bishop, Dynamical superfluid–insulator transition in a chain of weakly coupled Bose–Einstein condensates, *Phys. Rev. Lett.* 89(17), 170402 (2002)

160. M. Machholm, C. J. Pethick, and H. Smith, Band structure, elementary excitations, and stability of a Bose–Einstein condensate in a periodic potential, *Phys. Rev. A* 67(5), 053613 (2003)

161. M. Modugno, C. Tozzo, and F. Dalfovo, Role of transverse excitations in the instability of Bose–Einstein condensates moving in optical lattices, *Phys. Rev. A* 70(4), 043625 (2004)

162. A. J. Ferris, M. J. Davis, R. W. Geursen, P. B. Blakie, and A. C. Wilson, Dynamical instabilities of Bose–Einstein condensates at the band edge in one dimensional optical lattices, *Phys. Rev. A* 77, 012712 (2008)

163. S. Hooley and K. A. Benedict, Dynamical instabilities in a two-component Bose–Einstein condensate in a one dimensional optical lattice, *Phys. Rev. A* 75, 033621 (2007)

164. J. Ruostekoski and Z. Dutton, Dynamical and energetic instabilities in multicomponent Bose–Einstein condensates in optical lattices, *Phys. Rev. A* 76(6), 063607 (2007)

165. G. Barontini and M. Modugno, Instabilities of a matter wave in a matter grating, *Phys. Rev. A* 80(6), 063613 (2009)

166. S. Burger, F. S. Cataliotti, C. Fort, F. Minardi, M. Inguscio, M. L. Chiofalo, and M. P. Tosi, Superfluid and dissipative dynamics of a Bose–Einstein condensate in a periodic optical potential, *Phys. Rev. Lett.* 86(20), 4447 (2001)

167. L. Fallani, L. De Sarlo, J. E. Lye, M. Modugno, R. Saers, C. Fort, and M. Inguscio, Observation of dynamical instability for a Bose–Einstein condensate in a moving 1D optical lattice, *Phys. Rev. Lett.* 93, 140406 (2004)

168. J. Mun, P. Medley, G. K. Campbell, L. G. Marcassa, D. E. Pritchard, and W. Ketterle, Phase diagram for a Bose–Einstein condensate moving in an optical lattice, *Phys. Rev. Lett.* 99(15), 150604 (2007)

169. T. Ozawa, L. P. Pitaevskii, and S. Stringari, Supercurrent and dynamical instability of spin–orbit-coupled ultracold Bose gases, *Phys. Rev. A* 87(6), 063610 (2013)

170. P. Cladé, S. Guellati-Khélifa, F. Nez, and F. Biraben, Large momentum beam splitter using Bloch oscillations, *Phys. Rev. Lett.* 102(24), 240402 (2009)

171. Z. Chen and Z. Liang, Ground-state phase diagram of a spin–orbit-coupled bosonic superfluid in an optical lattice, *Phys. Rev. A* 93(1), 013601 (2016)

172. G. Juzeliūnas, J. Ruseckas, and J. Dalibard, Generalized Rashba–Dresselhaus spin–orbit coupling for cold atoms, *Phys. Rev. A* 81(5), 053403 (2010)

173. D. L. Campbell, G. Juzeliūnas, and I. B. Spielman, Realistic Rashba and Dresselhaus spin-orbit coupling for neutral atoms, *Phys. Rev. A* 84(2), 025602 (2011)

174. B. M. Anderson, G. Juzeliūnas, V. M. Galitski, and I. B. Spielman, Synthetic 3D spin–orbit coupling, *Phys. Rev. Lett.* 108, 235301 (2012)

175. Z. F. Xu, L. You, and M. Ueda, Atomic spin–orbit coupling synthesized with magnetic-field-gradient pulses, *Phys. Rev. A* 87(6), 063634 (2013)

176. B. M. Anderson, I. B. Spielman, and G. Juzeliūnas, Magnetically generated spin–orbit coupling for ultracold atoms, *Phys. Rev. Lett.* 111, 125301 (2013)

177. G. Juzeliūnas, J. Ruseckas, M. Lindberg, L. Santos, and P. Öhberg, Quasirelativistic behavior of cold atoms in light fields, *Phys. Rev. A* 77, 011802(R) (2008)

178. Chuanwei Zhang, Spin–orbit coupling and perpendicular Zeeman field for fermionic cold atoms: Observation of the intrinsic anomalous Hall effect, *Phys. Rev. A* 82, 021607(R) (2010)